Binary droplet collision simulations by a multiphase cascaded lattice Boltzmann method

Daniel Lycett-Brown, Kai H. Luo, Ronghou Liu, and Pengmei Lv

Articles you may be interested in

Study for optical manipulation of a surfactant-covered droplet using lattice Boltzmann method
Biomicrofluidics 8, 024104 (2014); 10.1063/1.4868368

Droplet spreading on a porous surface: A lattice Boltzmann study
Phys. Fluids 24, 042101 (2012); 10.1063/1.3701996

Wetting gradient induced separation of emulsions: A combined experimental and lattice Boltzmann computer simulation study
Phys. Fluids 20, 072104 (2008); 10.1063/1.2963958

Simulations of binary drop collisions with a multiple-relaxation-time lattice-Boltzmann model
Phys. Fluids 17, 122105 (2005); 10.1063/1.2148987

Numerical simulation of binary liquid droplet collision
Phys. Fluids 17, 082105 (2005); 10.1063/1.2009527

Binary droplet collision simulations by a multiphase cascaded lattice Boltzmann method

Daniel Lycett-Brown,[1] Kai H. Luo,[2,a)] Ronghou Liu,[3] and Pengmei Lv[4]

[1]*Energy Technology Research Group, Faculty of Engineering and the Environment, University of Southampton, Southampton SO17 1BJ, United Kingdom*
[2]*Department of Mechanical Engineering, University College London, Torrington Place, London WC1E 7JE, United Kingdom*
[3]*Biomass Energy Engineering Research Centre, School of Agriculture and Biology, Shanghai Jiao Tong University, 800 Dongchuan Road, Shanghai 200240, People's Republic of China*
[4]*Guangzhou Institute of Energy Conversion, Chinese Academy of Sciences, Guangzhou 510640, People's Republic of China*

Three-dimensional binary droplet collisions are studied using a multiphase cascaded lattice Boltzmann method (LBM). With this model it is possible to simulate collisions with a Weber number of up to 100 and a Reynolds number of up to 1000, at a liquid to gas density ratio of over 100. This is made possible by improvements to the collision operator of the LBM. The cascaded LBM in three dimensions is introduced, in which additional relaxation rates for higher order moments, defined in a co-moving reference frame, are incorporated into the collision operator. It is shown that these relaxation rates can be tuned to reduce spurious velocities around curved phase boundaries, without compromising the accuracy of the simulation results. The range of attainable Reynolds numbers is therefore increased. Different outcomes from both head-on and off-centre collisions are simulated, for both equal and unequal size droplets, including coalescence, head-on separation, and off-centre separation. For head-on collisions the critical Weber number between coalescence and separation is shown to decrease with decreasing ambient gas pressure. The variation of critical Weber number with droplet size ratio is also studied. Comparisons are made with the theoretical predictions of Tang *et al.* ["Bouncing, coalescence, and separation in head-on collision of unequal-size droplets," Phys. Fluids **24**, 022101 (2012)], and the effect of ambient gas pressure is again considered. For off-centre collisions, boundaries between different collision outcomes are accurately defined and quantitative comparisons are made with the theoretical predictions of Rabe *et al.* ["Experimental investigation of water droplet binary collisions and description of outcomes with a symmetric Weber number," Phys. Fluids **22**, 047101 (2010)]. While general agreement between the simulated and theoretical boundaries is presented, deviations due to varying liquid viscosity are observed. Finally, the prediction of the independence of regime boundaries with varying droplet size ratio, when using the symmetric Weber number as defined by Rabe *et al.*, is discussed. Simulation results showing qualitative agreement are presented, although some discrepancies are reported. © *2014 Author(s). All article content, except where otherwise noted, is licensed under a Creative Commons Attribution 3.0 Unported License.* [http://dx.doi.org/10.1063/1.4866146]

I. INTRODUCTION

The lattice Boltzmann method (LBM) is a rapidly developing approach to computational fluid dynamics (CFD). It has been successfully applied to a variety of problems, including (but not

---

a)Electronic mail: K.Luo@ucl.ac.uk

26, 023303-1 © Author(s) 2014

limited to) turbulence, micro flows, flows through porous media, magnetohydrodynamics, and both multiphase and multi-component systems (see, for example, Refs. 1–3 and references therein). Instead of solving the macroscopic Navier-Stokes equations as in traditional CFD, the LBM works on the mesoscopic scales, solving a discretised Boltzmann equation, designed to recover the Navier-Stokes equations in the macroscopic limit. As the LBM works with particle distribution functions, complex macroscopic fluid behaviours which occur as a result of particle interactions, such as phase separation, can be easily included. As interfaces between high and low density phases arise naturally, no interface tracking is required, representing a significant advantage over traditional CFD methods for multiphase flows. Here this method is applied to the modelling of binary droplet collisions.

In its simplest form the LBM uses a single relaxation time Bhatnagar-Gross-Krook (BGK) collision operator. It has been extensively shown in the single phase case that a significant improvement in attainable Reynolds number (Re) can be obtained through the use of a multiple relaxation time (MRT) collision operator.[4–7] Instead of relaxing particle distribution functions towards their equilibrium distribution functions, a transformation is made into moment space, where individual moments can be relaxed independently. The relaxation rates of higher order moments can then be used to increase stability. On a similar theme, Geier *et al.*[8] proposed the cascaded LBM, in which the collision operator relaxes moments in a co-moving reference frame, and showed improvements over results obtained using the MRT collision operator. Recently, we have developed a multiphase cascaded LBM and shown that this also provides significant improvement over the lattice BGK (LBGK) method, in terms of both reducing the spurious velocities around curved interfaces, and increasing the stability range for high Reynolds numbers.[9] Here this is extended to 3D and again significant improvements over the LBGK model are shown. In the 2D case we have shown that for the specific case of calculating the multiphase force term with the Shan-Chen model[10, 11] and incorporating this into the collision operator using the exact difference method (EDM),[12] these improvements are of the same order as those of the more established MRT method. Comparisons with the MRT method in the 3D case are therefore not made here. The lower spurious velocities and higher attainable Reynolds numbers allow us to simulate a wide range of droplet collision parameters.

The study of binary droplet collisions has many important applications across different scientific disciplines, from understanding cloud formation in climate theory, to engineering applications, such as turbine blade cooling, ink-jet printing, spray coating, and spray combustion in diesel internal combustion engines. For example, in spray in internal combustion engines, there exists a debate on what effect the viscosity of the fuel has on its combustion. On the one hand, higher viscosity increases the penetration of spray, resulting in an increase in mixing between air and fuel, which has been reported to increase engine power;[13, 14] on the other hand, higher viscosity decreases atomisation and therefore surface area, resulting in a decrease in engine power.[15, 16] The outcomes of binary droplet collisions within such spray depend on the liquid viscosity, therefore this has implications for the production of bio-diesel which generally has higher viscosities than recommended diesel standards. Consequently there exists a significant amount of experimental research on such collisions, from which a range of different collision outcomes have been identified, as shown in Fig. 1.[17] Ashgriz and Poo[18] studied the coalescence, head-on separation, and off-centre separation of water droplets up to a Weber number (We) of 100, and developed theoretical models for the boundaries between these regimes. Qian and Law[17] extended this study to include the bouncing regime, and analysed the effects on this regime of both gas pressure and viscosity, and the presence of liquid vapour in the gas. More recently, Rabe *et al.*[19] and Tang *et al.*[20] have studied the effect of unequal droplet size, while Pan *et al.*[21] have extended the Weber number up to 1000, and observed droplet splattering and breakup.

A number of different methods have been employed in the simulation of droplet collisions. Pan and Suga[22] used a finite volume scheme, and simulated collisions up to We = 150 and Re = 1300, but reported a mass loss of around 5%. Using a level set method Tanguy and Berlemont[23] achieved a similar parameter range, but with a mass loss less than 1% in the case of a very fine grid. However, the required level of grid refinement becomes impractical in 3D. Nikolopoulos and Bergeles[24] used a volume of fluid method, and studied the effects of both the liquid and gas properties on droplet collision outcome, however this method requires defining an artificial collision time. A number of different LBM approaches have also been applied, Inamuro *et al.*[25] used the projection
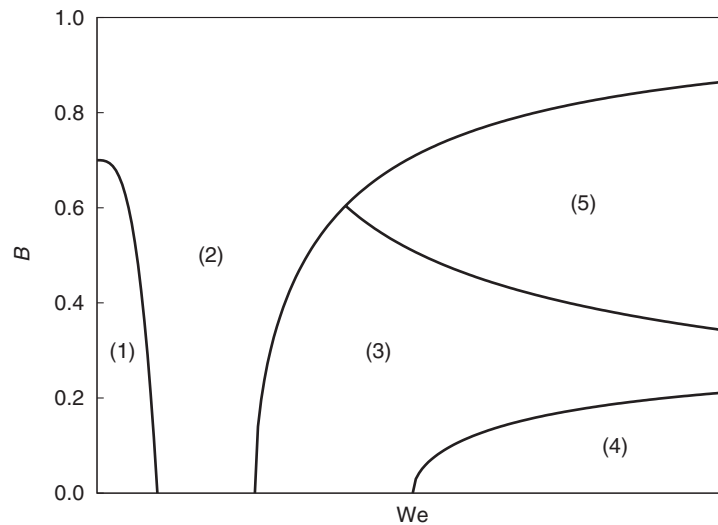
FIG. 1. Binary droplet collision outcomes for Weber number against impact parameter, B, as defined in Sec. IV C, (1) coalescence after minor deformation, (2) bouncing, (3) coalescence after substantial deformation, (4) near head-on separation, and (5) off-centre separation (after Ref. 17).

method applied to the free energy model, producing results for droplet collision at Re = 2000 and at We = 100. However, while it is stated that their method can reach a density ratio between the liquid and gas phase of up to 1000, the droplet collision results are only given at a ratio of 50. Luo *et al.*[26] used the Shan-Chen single component multiphase method with a MRT scheme, achieving Reynolds numbers of up to a few hundred, and Weber number up to 100, but again at a density ratio of approximately 50. Focke and Bothe[27] recently showed that under-resolution in some of these schemes results in artificial lamella breakup (see, for example, Ref. 23). A scheme is therefore required that can simulate high density ratios, high Reynolds numbers, and high Weber numbers simultaneously, while maintaining high resolution and avoiding mass loss. This is the ultimate goal of the work presented here.

We first present in Sec. II a derivation of the 3D cascaded LBM. The extension to multiphase, using the exact difference method,[12] is then given in Sec. III. Validation of the method and reductions in spurious velocities are discussed in Secs. IV A and IV B, respectively, before results for binary droplet collisions are presented in Sec. IV C.

II. CASCADED LBM

The cascaded LBM was developed to overcome some of the limitations of the MRT method. While the MRT method significantly enhances stability at low viscosity compared to the BGK method, it still suffers from instability at sufficiently low viscosities. Two potential sources of this instability were identified and resolved by the cascaded LBM.[8] The first of these was insufficient Galilean invariance, arising as a result of relaxing raw moments defined in the reference frame of a fixed lattice. This is resolved by relaxing central moments, which are defined in a reference frame that moves with the fluid. Specifically, it is required that the terms of third order in velocity in the third order moments are kept. With these terms included a second order error in viscosity is removed. In the 2D multiphase case we have shown that without these third order terms, varying the relaxation rate of the third order moment introduces an error into the multiphase result (in this case altering the period of droplet oscillation), these terms are therefore included throughout the following. Although the MRT method is usually truncated at second order in velocity this is not an inherent defect, and these third order terms should also be included in MRT implementations. The second source of instability was found to be a so-called "crosstalk" between moments. Central moments can be expressed in terms of raw moments, with central moments of a certain order only

containing terms of raw moments of that order and below. Relaxing a raw moment therefore affects higher order central moments, and it is this crosstalk between central moments that is suggested as a source of instability. This is overcome through relaxing moments in a cascade from lowest to highest order moment, the effect of the relaxation of a raw moment on a higher order central moment being known and removed before that higher order moment is itself relaxed.

The derivation follows that for the 2D cascaded LBM presented by Lycett-Brown and Luo,[9] beginning with the moment representation of populations (see, for example, Ref. 4). These are translated into their central moment form, before each central moment is independently relaxed. The three dimensional, 27 velocity lattice is used, with velocities $v_{(i,j,k)} = (v_{(i)}, v_{(j)}, v_{(k)})$. This is constructed as the tensor product of the velocities from the sets of three one-dimensional, three velocity lattices, with $v_{(i)} = i$, where $i = 0, \pm 1$. Moments of this product lattice can be written as[28]

$$\rho M_{pqr} = \langle f_{(i,j,k)} v_{(i)}^p v_{(j)}^q v_{(k)}^r \rangle, \ \ p, q, r \in \{0, 1, 2\}, \tag{1}$$

where $\langle ... \rangle$ represents summation over all of the velocity indices. In this notation $M_{000} = 1$ is the normalised density, and M_{100}, M_{010}, and M_{001} are the x, y, and z velocities (u_x, u_y, and u_z), respectively. The trace of the pressure tensor, T, and two normal stress differences, N_{xz} and N_{yz} (all at unity density), are defined as

$$T = M_{200} + M_{020} + M_{002},$$
$$N_{xz} = M_{200} - M_{002}, \tag{2}$$
$$N_{yz} = M_{020} - M_{002}.$$

$\Pi_{xy} = M_{110}$, $\Pi_{xz} = M_{101}$, and $\Pi_{yz} = M_{011}$ are the off-diagonal elements of the pressure tensor (at unit density). The third order moments are written as $Q_{xxy} = M_{210}$, $Q_{xxz} = M_{201}$, $Q_{xyy} = M_{120}$, $Q_{yyz} = M_{021}$, $Q_{xzz} = M_{102}$, $Q_{yzz} = M_{012}$, and $Q_{xyz} = M_{111}$, and the fourth order moments as $A_{xxyy} = M_{220}$, $A_{xxzz} = M_{202}$, and $A_{yyzz} = M_{022}$. Populations can be expressed in terms of these moments as

$$f_{(0,0,0)} = \rho \left[1 - T + A_{xxyy} + A_{xxzz} + A_{yyzz} - M_{222} \right],$$

$$f_{(\sigma,0,0)} = \frac{\rho}{2} \left[\sigma u_x + \frac{2}{3} N_{xz} - \frac{1}{3} N_{yz} + \frac{1}{3} T - \sigma Q_{xyy} - \sigma Q_{xzz} - A_{xxyy} - A_{xxzz} + \sigma M_{122} + M_{222} \right],$$

$$f_{(0,\lambda,0)} = \frac{\rho}{2} \left[\lambda u_y - \frac{1}{3} N_{xz} + \frac{2}{3} N_{yz} + \frac{1}{3} T - \lambda Q_{xxy} - \lambda Q_{yzz} - A_{xxyy} - A_{yyzz} + \lambda M_{212} + M_{222} \right],$$

$$f_{(0,0,\delta)} = \frac{\rho}{2} \left[\delta u_z - \frac{1}{3} N_{xz} - \frac{1}{3} N_{yz} + \frac{1}{3} T - \delta Q_{xxz} - \delta Q_{yyz} - A_{xxzz} - A_{yyzz} + \delta M_{221} + M_{222} \right],$$

$$f_{(\sigma,\lambda,0)} = \frac{\rho}{4} \left[\sigma\lambda \Pi_{xy} + \lambda Q_{xxy} + \sigma Q_{xyy} + A_{xxyy} - \sigma\lambda M_{112} - \lambda M_{212} - \sigma M_{122} - M_{222} \right],$$

$$f_{(\sigma,0,\delta)} = \frac{\rho}{4} \left[\sigma\delta \Pi_{xz} + \delta Q_{xxz} + \sigma Q_{xzz} + A_{xxzz} - \sigma\delta M_{121} - \delta M_{221} - \sigma M_{122} - M_{222} \right],$$

$$f_{(0,\lambda,\delta)} = \frac{\rho}{4} \left[\lambda\delta \Pi_{yz} + \delta Q_{yyz} + \lambda Q_{yzz} + A_{yyzz} - \lambda\delta M_{211} - \delta M_{221} - \lambda M_{212} - M_{222} \right],$$

$$f_{(\sigma,\lambda,\delta)} = \frac{\rho}{8} \left[\sigma\lambda\delta Q_{xyz} + \lambda\delta M_{211} + \sigma\delta M_{121} + \sigma\lambda M_{112} + \delta M_{221} + \lambda M_{212} + \sigma M_{122} + M_{222} \right],$$

$$\tag{3}$$

where $\sigma, \lambda, \delta = \{-1, 1\}$. Central moments are defined as in Geier *et al.*[8] as

$$\rho \tilde{M}_{pqr} = \left\langle f_{(i,j,k)} (v_{(i)} - u_x)^p (v_{(j)} - u_y)^q (v_{(k)} - u_z)^r \right\rangle. \tag{4}$$

After some algebra, the raw moments can be expressed in terms of central moments, these are given in Appendix A. They can be substituted into Eq. (3) to give populations expressed in terms of central moments. With the populations written in this form, a collision operator with independent relaxation rates for each central moment can be derived. The LBM is written as

$$f_{(i,j,k)} \left(\boldsymbol{x} + \boldsymbol{v}_{(i,j,k)}, t + 1 \right) = f_{(i,j,k)}^* (\boldsymbol{x}, t), \tag{5}$$

where collisions are written in the familiar form

$$f^*_{(i,j,k)} = (1-\omega)f_{(i,j,k)} + \omega f^{eq}_{(i,j,k)}. \tag{6}$$

The equilibrium values for the moments are given by[28]

$$\tilde{\Pi}^{eq}_{\alpha\beta} = 0,$$

$$\tilde{N}^{eq}_{xz} = \tilde{N}^{eq}_{yz} = 0,$$

$$\tilde{T}^{eq} = 3c^2_s,$$

$$\tilde{Q}^{eq}_{\alpha\alpha\beta} = 0,$$

$$\tilde{Q}^{eq}_{xyz} = 0, \tag{7}$$

$$\tilde{A}^{eq}_{\alpha\alpha\beta\beta} = c^4_s,$$

$$\tilde{M}^{eq}_{\alpha\alpha\beta\gamma} = 0,$$

$$\tilde{M}^{eq}_{\alpha\alpha\beta\beta\gamma} = 0,$$

$$\tilde{M}^{eq}_{xxyyzz} = c^6_s,$$

where α, β, $\gamma \in \{x, y, z\}$ and $c^2_s = 1/3$ is the speed of sound squared. The relaxation rate for the trace of the pressure tensor, T, can be replaced by ω_b, relating to the bulk viscosity, and the relaxation rates for the third and fourth order moments, given by Q and A, replaced by ω_3 and ω_4, respectively. This allows the bulk viscosity to be set independently of the kinematic viscosity, ν, and the higher order moments to be relaxed independently. For the Q_{xyz}, $M_{\alpha\alpha\beta\gamma}$, fifth, and sixth order moments ω is set equal to 1. Using the equilibrium values of the moments, this leads to

$$
\begin{aligned}
f^*_{(0,0,0)} = \rho\Bigg[&\frac{26}{27} - u^2 + 4u_x u_y \tilde{\Pi}^*_{xy} + 4u_x u_z \tilde{\Pi}^*_{xz} + 4u_y u_z \tilde{\Pi}^*_{yz} \\
&+ \frac{1}{3}\left(-2u^2_x + u^2_y + u^2_z\right)\tilde{N}^*_{xz} + \frac{1}{3}\left(u^2_x - 2u^2_y + u^2_z\right)\tilde{N}^*_{yz} + \left(\frac{2}{3}u^2 - 1\right)\tilde{T}^* \\
&+ 2u_y\left(1 - u^2_z\right)\tilde{Q}^*_{xxy} + 2u_z\left(1 - u^2_y\right)\tilde{Q}^*_{xxz} + 2u_x\left(1 - u^2_z\right)\tilde{Q}^*_{xyy} \\
&+ 2u_z\left(1 - u^2_x\right)\tilde{Q}^*_{yyz} + 2u_x\left(1 - u^2_y\right)\tilde{Q}^*_{xzz} + 2u_y\left(1 - u^2_x\right)\tilde{Q}^*_{yzz} \\
&+ \left(1 - u^2_z\right)\tilde{A}^*_{xxyy} + \left(1 - u^2_y\right)\tilde{A}^*_{xxzz} + \left(1 - u^2_x\right)\tilde{A}^*_{yyzz}\Bigg],
\end{aligned}
\tag{8}
$$

where terms of fourth order and higher in velocity have been dropped, $\tilde{Q}^*_{xyz} = 0$, $\tilde{M}^*_{\alpha\alpha\beta\gamma} = 0$, $\tilde{M}^*_{\alpha\alpha\beta\beta\gamma} = 0$, and $\tilde{M}^*_{xxyyzz} = 1/27$ have been used, and

$$\tilde{\Pi}^*_{\alpha\beta} = (1-\omega)\tilde{\Pi}_{\alpha\beta},$$

$$\tilde{N}^*_{xz} = (1-\omega)\tilde{N}_{xz},$$

$$\tilde{N}^*_{yz} = (1-\omega)\tilde{N}_{yz},$$

$$\tilde{T}^* = (1-\omega_b)\tilde{T} + \omega_b, \tag{9}$$

$$\tilde{Q}^*_{\alpha\beta\beta} = (1-\omega_3)\tilde{Q}_{\alpha\beta\beta},$$

$$\tilde{A}^*_{\alpha\alpha\beta\beta} = (1-\omega_4)\tilde{A}_{\alpha\alpha\beta\beta} + \frac{1}{9}\omega_4.$$

Expressions for the other post-collision distribution functions are given in Appendix B. As shown in Geier *et al.*,[29] the third order terms in velocity are required to maintain Galilean invariance. It was further shown for the 2D multiphase case that these terms were required to allow the relaxation rate of the third order moment to be varied without affecting results,[9] they are therefore

included both in the collision operator, Eq. (8), and in the EDM as described in Sec. III. Under the constraint of $\omega_b = \omega_3 = \omega_4 = \omega$, Eq. (8) recovers the BGK form of the collision operator to second order in velocity. Using the Chapman-Enskog multi-scales expansion, it can be shown that this scheme recovers the isothermal Navier-Stokes equations at reference temperature $T_0 = c_s^2$:

$$\partial_t \rho + \partial_\alpha (\rho u_\alpha) = 0, \tag{10}$$

$$\partial_t u_\alpha + u_\beta \partial_\beta u_\alpha + \frac{1}{\rho} \partial_\alpha (c_s^2 \rho) - \frac{1}{\rho} \partial_\beta \left[\nu \rho \left(\partial_\alpha u_\beta + \partial_\beta u_\alpha - \frac{2}{3} \delta_{\alpha\beta} \partial_\gamma u_\gamma \right) \right]$$
$$- \frac{2}{3\rho} \partial_\alpha \left(\xi \rho \partial_\gamma u_\gamma \right) = 0, \tag{11}$$

where

$$\nu = \left(\frac{1}{\omega} - \frac{1}{2} \right) c_s^2, \ \xi = \left(\frac{1}{\omega_b} - \frac{1}{2} \right) c_s^2 \tag{12}$$

are the kinematic and bulk viscosities.

III. MULTIPHASE METHOD

A number of methods for including multiphase behaviour into the LBM have been proposed, including the free-energy models,[30–32] those based on the kinetic theory of dense fluids,[33–35] and the interaction potential models[10,11,36] which are used here. Originally proposed by Shan and Chen[10] the interaction potential models calculate a force through a local interaction potential, which then modifies the velocity in the equilibrium distribution functions. Despite the success of the multiphase LBM, simulating flows with both a high density ratio between the liquid and gas phases and low viscosity remains challenging. One well known problem is the formation of spurious velocities around curved interfaces. A number of improvements to the interaction potential model have been proposed and can be divided into two categories: those that modify the force calculation, such as increasing the order of isotropy[37] or modifying the equation of state,[38] and those that improve the incorporation of the force term into the equilibrium distribution functions. The original Shan-Chen model introduced the forcing term into the LBM through modifying the momentum in the equilibrium distribution function, and it is well known that this leads to a scheme which is unstable for values of ω other than 1. Improvements to this method include the method of explicit derivatives, as used in the multiphase schemes derived from the kinetic theory of dense fluids,[33–35] the method of Guo *et al.*[39] which takes into account discrete lattice effects, and the EDM which is used here.[12] It has been shown recently that while the method of Guo *et al.* recovers the Navier-Stokes equations correctly, the EDM introduces an error into the pressure tensor, proportional to the square of the forcing term.[39,40] However, this analysis is based on a second order expansion of the LBM which has been shown to be insufficient to identify all relevant error terms when considering forces with large gradients, as are present at interfaces in multiphase schemes.[41] Results show that the EDM is stable over a larger range of density ratios than the method of Guo *et al.*,[39] and gives smaller errors for high density ratio multiphase systems.[9,12] Unlike other methods (see, e.g., Premnath and Banerjee[42]), the EDM does not modify the collision operator, allowing the cascaded LBM collision operator to be used in the form derived above.

As originally described by Kupershtokh *et al.*,[12] and discussed for the cascaded LBM by Lycett-Brown and Luo,[9] a forcing term can be incorporated into the LBM as

$$f_{(i,j,k)} \left(\mathbf{x} + \mathbf{v}_{(i,j,k)}, t+1 \right) = f_{(i,j,k)}^* (\mathbf{x}, t) + F_{(i,j,k)}, \tag{13}$$

in which

$$F_{(i,j,k)} = f_{(i,j,k)}^{eq} \left(\rho, \mathbf{u}' \right) - f_{(i,j,k)}^{eq} (\rho, \mathbf{u}), \tag{14}$$

where $\boldsymbol{u}' = \boldsymbol{u} + \Delta\boldsymbol{u}$ and $\Delta\boldsymbol{u} = \boldsymbol{F}\Delta t/\rho$. An important note is made on the form of f_i^{eq} used here. To third order, the BGK form is given by

$$f_i^{eq} = \rho w_i \left[1 + \frac{v_{i\alpha}u_\alpha}{T_0} + \frac{u_\alpha u_\beta}{2T_0^2} \left(v_{i\alpha}v_{i\beta} - T_0\delta_{\alpha\beta} \right) + \frac{u_\alpha u_\beta u_\gamma}{6T_0^3} v_{i\gamma} \left(v_{i\alpha}v_{i\beta} - 3T_0\delta_{\alpha\beta} \right) \right] + \mathcal{O}(u^4),$$
(15)

where w_i are weights given by $w_{(0,0,0)} = 8/27$, $w_{(\sigma,0,0)} = w_{(0,\lambda,0)} = w_{(0,0,\delta)} = 2/27$, $w_{(\sigma,\lambda,0)} = w_{(\sigma,0,\delta)} = w_{(\lambda,0,\delta)} = 1/54$, and $w_{(\sigma,\lambda,\delta)} = 1/216$. This contains terms of u_α^3, $u_\alpha^2 u_\beta$, and $u_x u_y u_z$, whereas in the BGK limit, the equilibria expressed in terms of central moments only contain third order terms of $u_\alpha^2 u_\beta$ and $u_x u_y u_z$. To second order in velocity the two forms of the equilibria are identical and Eq. (14) can be written explicitly as

$$F_i^{O(u^2)} = \rho w_i \left[\frac{\boldsymbol{v}_i - \boldsymbol{u}}{c_s^2} + \frac{(\boldsymbol{v}_i \boldsymbol{u})}{c_s^4} \boldsymbol{v}_i \right] \Delta\boldsymbol{u} + \rho w_i \left[\frac{(\boldsymbol{v}_i \Delta\boldsymbol{u})^2}{2c_s^4} - \frac{(\Delta\boldsymbol{u})^2}{2c_s^2} \right].$$
(16)

For the third order term, only those terms found in the moment form of the equilibria are included, giving

$$\begin{aligned}
F_i^{O(u^3)} = F_i^{O(u^2)} + \frac{9}{2}\rho w_i \Big[& (3v_{ix}^2 - 1)\left(v_{iy}(u_x'^2 u_y' - u_x^2 u_y) + v_{iz}(u_x'^2 u_z' - u_x^2 u_z) \right) \\
& + (3v_{iy}^2 - 1)\left(v_{ix}(u_x' u_y'^2 - u_x u_y^2) + v_{iz}(u_y'^2 u_z' - u_y^2 u_z) \right) \\
& + (3v_{iz}^2 - 1)\left(v_{ix}(u_x' u_z'^2 - u_x u_z^2) + v_{iy}(u_y' u_z'^2 - u_y u_z^2) \right) \\
& + 6v_{ix}v_{iy}v_{iz}\left(u_x' u_y' u_z' - u_x u_y u_z \right) \Big],
\end{aligned}$$
(17)

where $c_s^2 = 1/3$ has been used. With this modification to the LBM, the physical velocity of the fluid, $\hat{\boldsymbol{u}}$, is given by

$$\hat{\boldsymbol{u}} = \boldsymbol{u} + \frac{\boldsymbol{F}}{2\rho}.$$
(18)

This is the velocity used when discussing spurious velocities in Sec. IV, and is different from the velocity, $\boldsymbol{u}$, used in the equilibrium. Following the Shan-Chen model the force term is calculated as

$$\boldsymbol{F} = -G\psi(\boldsymbol{x}) \sum w_{(i,j,k)}\psi(\boldsymbol{x} + \boldsymbol{v}_{(i,j,k)})\boldsymbol{v}_{(i,j,k)}.$$
(19)

This force modifies the equation of state from that of an ideal gas to

$$P = \rho c_s^2 + \frac{G c_s^2}{2}\psi(\boldsymbol{x})^2,$$
(20)

where G controls the interaction strength and ψ is the effective mass. Sbragaglia *et al.*[37] showed that through rearranging the expression for ψ more realistic equations of state than the original Shan-Chen exponential form could be introduced, and that this significantly increased the density ratio attainable. The results given in Sec. IV use the Carnahan-Starling equation of state, given by

$$P^{CS} = \rho RT \frac{1 + \frac{b\rho}{4} + \left(\frac{b\rho}{4}\right)^2 - \left(\frac{b\rho}{4}\right)^3}{\left(1 - \frac{b\rho}{4}\right)^3} - a\rho^2,$$
(21)

where the constants are set to $R = 1$, $a = 1$, and $b = 4$ in an effective mass given by

$$\psi(\rho) = \sqrt{\frac{2\left(P^{CS} - \rho c_s^2\right)}{G c_s^2}}.$$
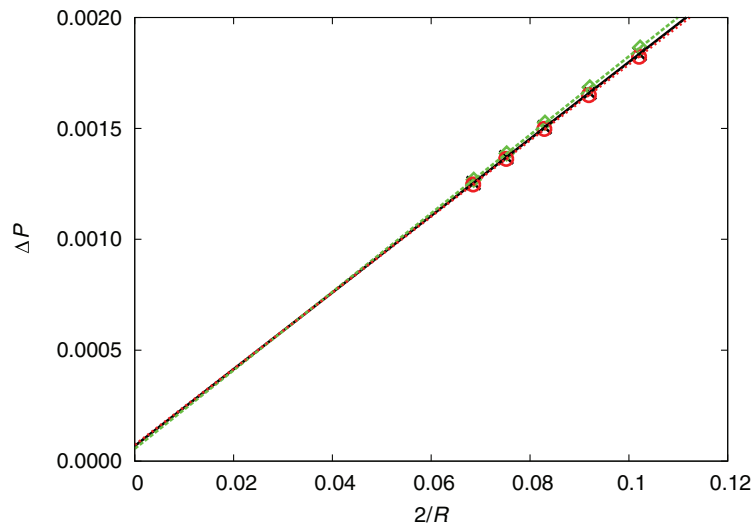(22)

FIG. 2. The Laplace law for varying ω_3, at $\omega = 1$, for $\omega_3 = 1$ (the third order LBGK method) (solid black lines), $\omega_3 = 0.4$ (dashed green lines), and $\omega_3 = 1.8$ (dotted red lines). The measured surface tensions are $\sigma = 0.0173$ for $\omega_3 = 1$, $\sigma = 0.0177$ for $\omega_3 = 0.4$, and $\sigma = 0.0172$ for $\omega_3 = 1.8$.

With ψ in this form the density ratio is no longer governed by G (now specified to keep the square root acting on a positive number), but by T.

IV. RESULTS

A. Validation

Before the cascaded LBM can be applied to the study of droplet collisions, validation of the method is required. The properties of the system, including density ratio, surface tension, and viscosity, are therefore studied under variation of the relaxation rates, first for a droplet in equilibrium and then for an oscillating droplet. The reductions in spurious velocities around a droplet in equilibrium are then presented for varying conditions. Results for droplet collisions are then presented.

The Laplace law is an important benchmark for droplets in equilibrium. It is given by

$$\Delta P = \frac{2}{R}\sigma, \tag{23}$$

where σ is the surface tension and R is the droplet radius in lattice units. Droplets of different radii, up to a maximum of $R = 30$, were initiated in the centre of a $96 \times 96 \times 96$ domain and simulations run to equilibrium. For this we set $T = 0.063$ giving a density ratio of approximately 100,[38] at both $\omega = 1$ ($v = 1/6$) and $v = 1/32$ (using the EDM the density ratio is constant for varying viscosity). This was repeated for different values of the relaxation parameters. For both $\omega = 1$ and $v = 1/32$ very little variation in the measured surface tension is seen when varying ω_b, ω_3, and ω_4 across their stable domains. For $\omega = 1$ the highest deviations in σ between the cascaded LBM and the LBGK method were 0.6%, 2.2%, and 0.2% at $\omega_b = 0.4$, $\omega_3 = 0.4$, and $\omega_4 = 0.2$, respectively. For $v = 1/32$ the result was similar, with maximum deviations being 0.3%, 1.3%, and 0.8% at $\omega_b = 1.2$, $\omega_3 = 0.4$, and $\omega_4 = 1.0$, respectively. The graph of the Laplace law for the case of varying ω_3 for $\omega = 1$ is given in Fig. 2.

The Laplace law results show that the relaxation rates can be varied across their whole stability range, without significantly affecting a droplet at equilibrium. One difference is that this equilibrium is reached sooner as ω_b tends to 0, and later as ω_b approaches 2 (this is unaffected by changes in the relaxation rates of the third and fourth order moments).
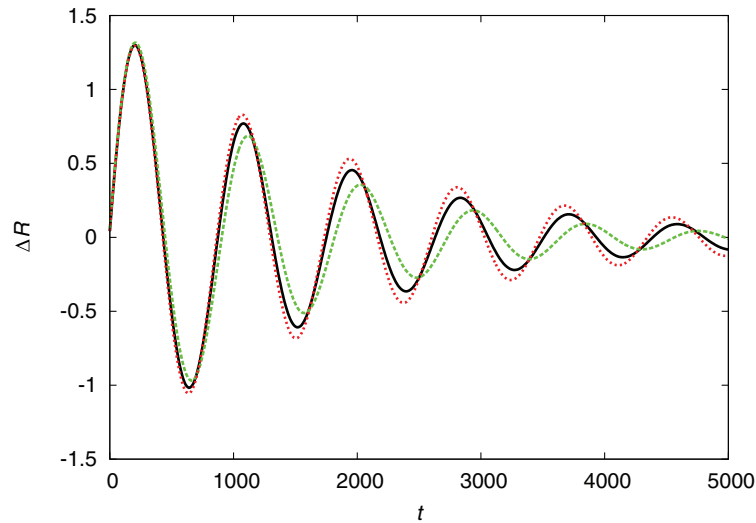
FIG. 3. Droplet oscillations showing the deviation of the interface from its position at equilibrium, ΔR (in lattice units), with time steps, t. Results shown are for $\nu = 1/32$ for the LBGK method (solid black lines), and the cascaded LBM with $\omega_b = 1.2$ (dashed green lines), and $\omega_b = 1.9$ (dotted red lines). The measured oscillation periods and decay rates are $T_o = 876.8$ and $\gamma = 5.92 \times 10^{-4}$ for the LBGK method, $T_o = 910.0$ and $\gamma = 7.10 \times 10^{-4}$ for the cascaded LBM with $\omega_b = 1.2$, and $T_o = 868.4$ and $\gamma = 5.07 \times 10^{-4}$ for the cascaded LBM with $\omega_b = 1.9$.

The case of an oscillating droplet is now considered. The same setup is used, with viscosity set to $\nu = 1/32$. Once droplets reached equilibrium an initial velocity was applied, given by

$$u_x = U_0 \frac{x - x_0}{R},$$
$$u_y = U_0 \frac{y - y_0}{R}, \tag{24}$$
$$u_z = -2U_0 \frac{z - z_0}{R},$$

for droplets centred at (x_0, y_0, z_0). Again, this was repeated across the stable domain of each relaxation parameter. Varying ω_3 and ω_4 produced no visible deviation in results, with maximum changes in oscillation period and decay rate of just 0.3% and 1.3%, respectively, at $\omega_3 = 0.4$. Figure 3 shows the result for varying the bulk viscosity, giving the deviation of the droplet interface from its position at equilibrium, along the x-axis. The changes in period and decay rate are 3.8% and 19.9% for $\omega_b = 1.2$, and 1.0% and 14.4% for $\omega_b = 1.9$. Oscillation period is related to surface tension, therefore varying ω_b can be seen to have a small effect on the surface tension, while the rate of decay is related to the viscosity of the system. As in the equilibrium case varying the relaxation rates of the third and fourth order moments has almost no effect on results, allowing these parameters to be used to tune the stability of the system.

B. Spurious velocities

The reduction in spurious velocities around droplets is now considered. It has been shown that the additional relaxation rates in the cascaded LBM can be varied without significantly affecting the multiphase results, therefore spurious velocities were measured for a wide range of combinations of these parameters. Droplets of radius 20 were set up in the centre of a $80 \times 80 \times 80$ domain, with a density ratio of 20 (using $T = 0.073$). The average spurious velocity magnitude in the gas phase, $\overline{u}_g$, defined as

$$\overline{u}_g = \frac{1}{X_g} \sum_{\text{gas}} \sqrt{\hat{u}_x^2 + \hat{u}_y^2}, \tag{25}$$
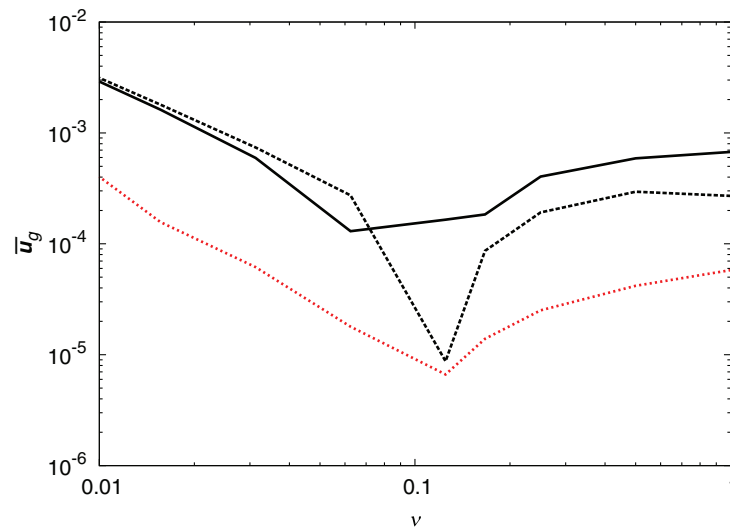
FIG. 4. Average magnitude of the spurious velocities in the gas phase, for varying viscosity, at a density ratio of 20. Results are for the LBGK method at second order (solid black line) and third order (dashed black line) and the minimum values are found from varying the additional relaxation rates of the cascaded LBM (dotted red line).

where the sum is over the X_g lattice sites containing the gas phase, was recorded once equilibrium had been reached (as discussed in Ref. 9, the use of $\overline{u}_g$ gives a better understanding of the reduction in the spurious velocities in the bulk of the gas, compared with the more often reported maximum spurious velocity, which usually occurs within the interface). This was repeated for varying all three relaxation parameters simultaneously, with each varied from 0.2 to 1.8 in intervals of 0.2 (a total of 729 simulations).

Figure 4 shows results for the minimum value found for the average spurious velocity in the gas around droplets, for a range of viscosities from 1 to 0.01. Results for the cascaded LBM are shown (which includes third order terms in velocity), along with the LBGK case for comparison, at both second and third orders. The reduction in spurious velocities compared with the second order LBGK method is roughly one order of magnitude across the whole range of viscosities. While this is slightly less than that observed in the 2D case, it is still a significant reduction. Taking, for example, 0.0001 as the maximum average spurious velocity in the gas which can be tolerated for a simulation, the usable range of both low and high viscosities is appreciably extended.

Fixing $\omega = 1$, Fig. 5 shows results for varying density ratio. It can be seen that the reductions in spurious velocities over the second order LBGK method at higher density ratios are slightly higher than those at a density ratio of 20, being almost two orders of magnitude above a density ratio of 100. Including the third order terms in the LBGK method has also given a much greater reduction in spurious velocities, although the cascaded LBM still outperforms this across the entire density ratio range.

The cascaded LBM has given significant reductions in spurious velocities compared with the LBGK method, across a wide range of viscosities and density ratios (as was the case for the previously reported 2D results), and has also extended the usable viscosity range. This model is therefore now used to simulate a range of binary droplet collisions.

C. Droplet collisions

Head-on droplet collisions will be specified here by two dimensionless parameters, the Weber number, a measure of the ratio of inertial to surface tension forces, and the Ohnesorge number, a measure of the ratio of viscous forces to inertial and surface tension forces. Droplet collisions that are studied here have Weber numbers significantly greater than one. For collisions with Weber number much less than one, especially around the boundary between bouncing and coalescence,
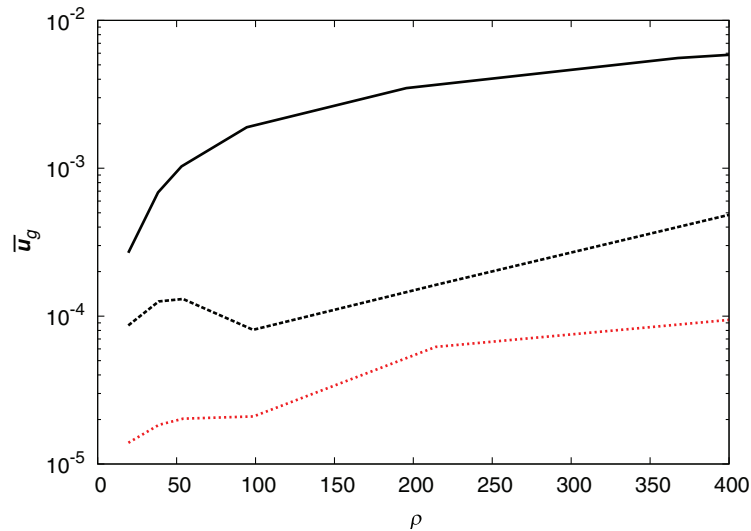
FIG. 5. Average magnitude of the spurious velocities in the gas phase, for varying density ratio, at $\omega = 1$. Results are for the LBGK method at second order (solid black line) and third order (dashed black line) and the minimum values are found from varying the additional relaxation rates of the cascaded LBM (dotted red line).

other dimensionless parameters such as Capillary number become important, as discussed by, for example, Gopinath and Koch.[43] Here the Weber number is defined as

$$\text{We} = \frac{2R_s \rho U^2}{\sigma},\tag{26}$$

where U is the relative droplet velocity, and the Ohnesorge number is defined as

$$\text{Oh} = \nu \sqrt{\frac{\rho}{2R_s \sigma}}.\tag{27}$$

This is related to the Reynolds number,

$$\text{Re} = \frac{2R_s U}{\nu},\tag{28}$$

by

$$\text{Oh} = \frac{\sqrt{\text{We}}}{\text{Re}},\tag{29}$$

therefore an alternative, and often used, choice is to define droplet collisions by Weber and Reynolds numbers. For the case of off-centre collisions, a third dimensionless parameter, the impact parameter, is required. This is defined as

$$B = \frac{\chi}{R_s + R_l},\tag{30}$$

where χ is the separation between the centres of the droplets, perpendicular to their direction of motion. In the case of unequally sized droplets subscripts s and l refer to the small and large droplets, respectively.

1. Head-on collisions of equal size droplets

For head-on droplet collisions ($B = 0$) the different collision outcomes observed experimentally, as shown in Fig. 1, in order of increasing Weber number, are coalescence after minor deformation, bouncing, coalescence after substantial deformation, and coalescence followed by separation.[44] Bouncing occurs due to a thin film of the gaseous phase becoming trapped between the flattening faces of the two approaching droplets. As the droplets approach each other, pressure in the gas
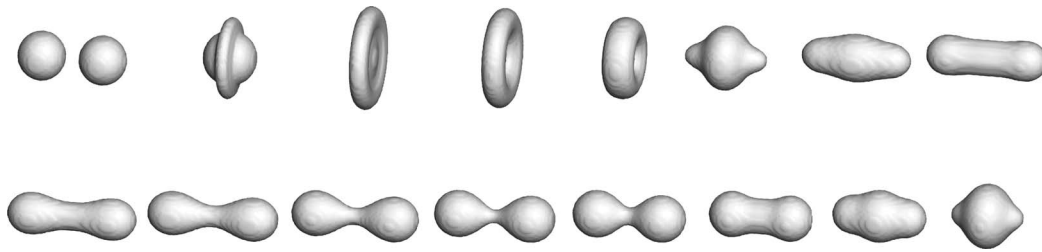
FIG. 6.   Head-on coalescence of equal sized droplets. We = 61.5, Re = 238.

increases causing the droplets to deform into an approximately hemispherical shape, with a flattening leading face. The ambient gas becomes trapped between these approaching faces. At very low Weber number the droplets do not deform greatly, therefore this trapping has less effect and droplets can coalesce. As Weber number is increased, greater deformation occurs, both increasing the conversion of kinetic energy into surface energy and increasing the pressure force between the droplets. If all kinetic energy is lost before the gap between the interfaces becomes sufficiently small for van der Waals forces to take effect, then the droplets relax under surface tension. This results in the droplets bouncing. Further increase in Weber number, while increasing deformation which promotes bouncing, increases the available kinetic energy. This allows the critical distance between the droplets to be reached, and coalescence to occur. A detailed analysis of this process can be found by Zhang and Law,[44] where the effects of gas density and viscosity are also analysed. Further dimensionless parameters other than the Ohnesorge and Weber numbers are required to specify the bouncing regime, including a capillary number which relates surface tension to the viscosity of the gas trapped between the droplets. As the distance between the approaching droplet faces becomes less than the mean free path of gas molecules, Knudsen number is also required.

No bouncing was observed with the present model, for which there are a number of possible reasons. First, it has been shown experimentally[17] that an increased proportion of liquid vapour in the gas can dramatically reduce the bouncing regime, and can remove (at least head-on) bouncing completely. As the current single component multiphase model consists of a liquid in its own vapour the likelihood of bouncing is reduced. The effect of the vaporised liquid in the gas was neglected in the study of Zhang and Law[44] and should be considered in future models. Second, there is an issue with resolving the intervening gas layer. For the approaching interfaces to merge they must come within the range of the van der Waals forces. This is usually of the order of tens of nanometres, about four orders of magnitude smaller than the typical droplet size of hundreds of micrometres. To resolve this gap in simulation, orders of magnitude higher resolution would be required (this could be possible with a mesh refinement technique, however this is not considered here). Finally, it should be noted that some other multiphase CFD models require the definition of an artificial collision time to specify if and when the two approaching interfaces should merge. This deficiency is not present in the current model, in which coalescence of the diffusive interfaces arises naturally. Further study, using increased resolution and a multi-component, multiphase model, is required to identify the bouncing regime.

A case of droplet coalescence is shown in Fig. 6. Unless otherwise stated, this and all following simulations were performed on a $512 \times 320 \times 320$ grid, with $T = 0.063$ giving a density ratio of approximately 120. For this case $\nu = 1/16$, and $\omega_b = 0.4$, $\omega_3 = 0.6$, and $\omega_4 = 0.4$.

As Weber number is further increased, the deformation of the coalesced droplet increases. The coalesced droplet initially forms an outward spreading disk. This disk eventually contracts under surface tension and the droplet then stretches out along the axis of initial coalescence in the shape of a dumbbell (essentially two liquid masses connected by a small ligament). If inertial forces exceed surface tension forces the ligament breaks, and the droplets separate, an example of which is shown in Fig. 7. As Weber number is further increased, an increasing number of smaller satellite droplets are formed from the breakup of the connecting ligament. Figure 8 shows the case of three satellite droplets, at We = 101 and Re = 1190. It has also been shown
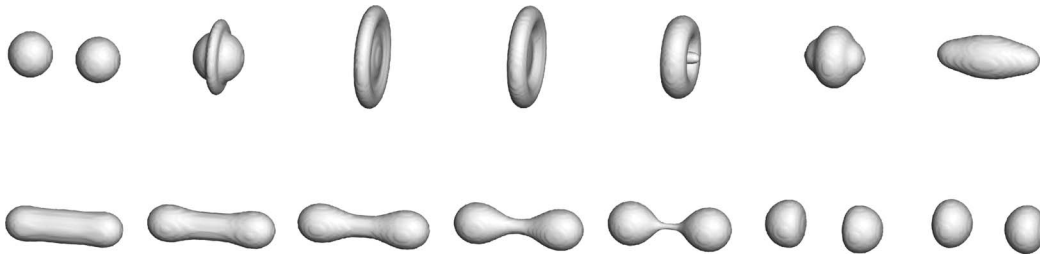
FIG. 7. Head-on separation of equal sized droplets. We = 83.3, Re = 277.
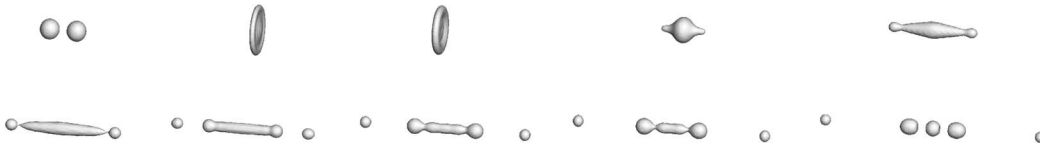
FIG. 8. Head-on separation of equal sized droplets creating three satellite droplets. We = 101, Re = 1190.
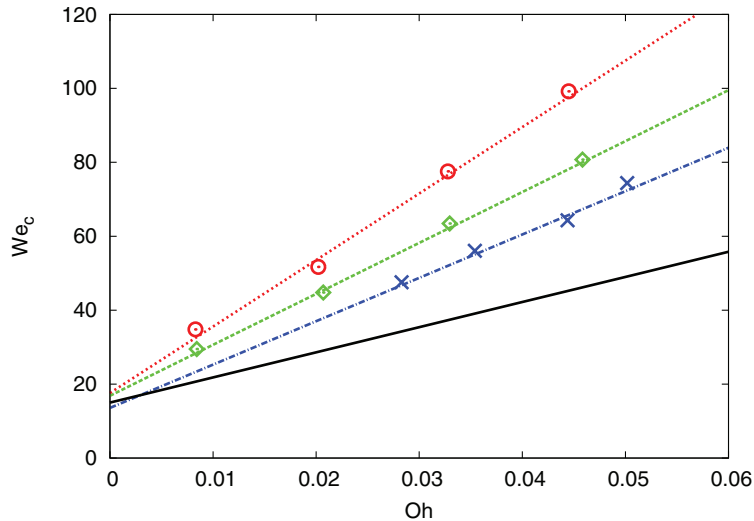
FIG. 9. Critical Weber number with varying Ohnesorge for a density ratio of approximately 64 (red circles), 128 (green diamonds), and 256 (blue crosses). The solid black line shows the experimental result from Qian and Law.[17]

experimentally that increasing the Weber number to $O(1000)$ results in other collision phenomena such as splattering.[21]

These results are in good qualitative agreement with those of Qian and Law.[17] To analyse the results further, the critical Weber number between droplet coalescence and separation, We_c, is considered. As described above, droplets separate when inertial forces overcome those of surface tension. Based on energy conservation, Qian and Law[17] derived a relationship for the critical Weber number. By considering initial kinetic energy, surface energy, and viscous dissipation, they derived an equation for We_c as

$$We_c = \beta Oh + \gamma. \tag{31}$$

From experimental results, the values of β and γ were found to be 680 and 15, respectively. Figure 9 shows the cascaded LBM simulation results and this experimental result. Points represent boundaries between coalescence and separation (from varying U in intervals of 0.002 at fixed Oh, the plotted points being the midpoints between the two cases). The results show the correct linear relationship between the Ohnesorge number and critical Weber number. The offsets from the origin, which are
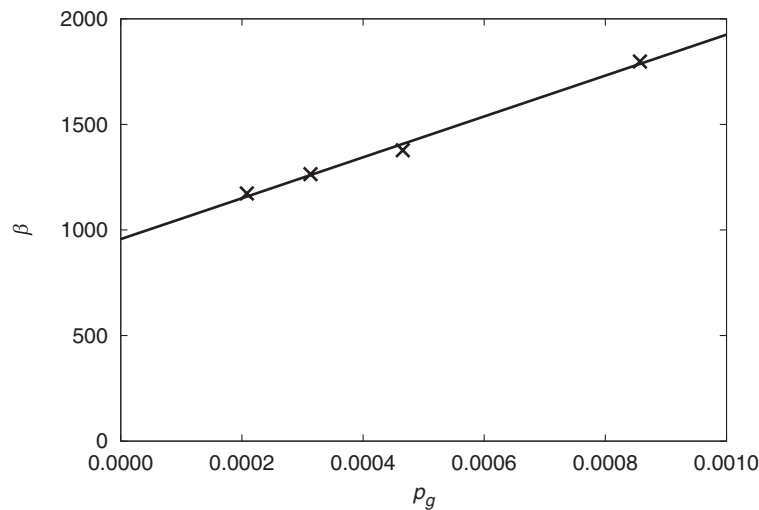
FIG. 10. Measured values of the gradients, β, of the We$_c$ against Oh plots shown in Fig. 9, against gas pressure, showing convergence to $\beta = 960$ in the limit of zero gas pressure ($\beta = 680$ from experimental data[17]).

related to the extra surface energy of a deformed droplet surface, are also in good agreement. However, it can be seen that the LBM results give a higher critical Weber number at a given Ohnesorge number. There are a number of possible reasons for the observed error in the LBM results. In developing their theoretical model, Qian and Law[17] neglect the gas phase. This is reasonable due to the low pressure and viscosity of the gas. However, from the discussion of droplet bouncing, as the droplets approach and the gas is squeezed between them, it is known that gas pressure and viscosity can play a role. Experimentally, this is usually only significant in the low Weber number bouncing regime.[43] However, one significant issue with the LBM is the density ratio between the liquid and gas phases. Here the maximum density ratio used is 256, which compares with a density ratio of about 1000 for water droplets colliding in air at atmospheric pressure. The pressure in the gas is significantly higher in the LBM simulations than the experimental results. Figure 9 shows results for three different density ratios. Decreasing the relative gas pressure (by increasing the density ratio) reduces the error in the LBM results, which shows that the properties of the gas are significantly affecting the results. The gradients of linear fits to the data are plotted against gas pressure in Fig. 10. From this the gradient for negligible gas pressure can be extrapolated, and is found to be 960.

While density ratio has been found to play a significant role, this is still 41% larger than the experimentally observed value. This additional error may be due to a number of factors, suggestions for which are now offered. Insufficient mesh resolution is known to effect collision outcomes, the main source of error coming from the width of the diffusive interface being orders of magnitude too large. This prevents proper resolution of the gas layer between approaching droplets. Further effects could include resolution of the thin liquid bridge connecting droplets before separation. While experimentally gas viscosity can be neglected, here it could play a role. In the multiphase LBM used here the gas kinematic viscosity is equal to the liquid kinematic viscosity and therefore increases linearly with increasing Ohnesorge number. Dissipation of energy to the gas depends on the gas dynamic viscosity. As Ohnesorge number increases (at fixed density ratio), gas dynamic viscosity also increases. At constant Ohnesorge number (constant ν) increasing gas density also increases gas dynamic viscosity. These increases in dynamic viscosity slightly increase energy dissipation to the gas, which could lead to a higher critical Weber number at higher Ohnesorge number and lower density ratio. Additional error could come from the use of bulk viscosity for stability, and spurious velocities, as discussed above. Further work to clarify the source of error and consequently improve the multiphase LBM should be the subject of future work.

2. Head-on collisions of unequal size droplets

Tang *et al.*[20] recently derived a generalisation of Eq. (31) to include droplets of unequal size, which they found to be in good agreement with their experimental results. For their derivation they use similar energy considerations as used by Qian and Law[17] in deriving the relationship between critical Weber number and Ohnesorge number in the equal sized droplet case. Defining the droplet size ratio as

$$\Delta = \frac{R_s}{R_l}, \tag{32}$$

then Eq. (31) becomes

$$\mathrm{We_c} = \beta(\Delta)\mathrm{Oh} + \gamma(\Delta), \tag{33}$$

where β and γ are now dependent on Δ. The form of these variables and details of their derivation can be found in the original paper.[20] As in the equal size droplet case, the point of separation is determined by considering the balance of energy. Separation occurs when the droplets have enough initial kinetic energy to overcome viscous dissipation and the additional surface tension energy associated with the deformed drops at the point of separation. The viscous dissipation is considered in three stages, the first being the point from initial coalescence to maximum deformation in the direction perpendicular to the collision axis, the second being from this point up until the droplet returns to a near-spherical shape, and the final stage being the stretching of this sphere back out along the axis of collision. The viscous losses in each stage were calculated separately, and it was shown that the majority of the difference in critical Weber number as size ratio is changed comes from the second stage. In this stage viscous losses increase as size ratio decreases. Higher initial kinetic energy is therefore required for separation, giving an increased critical Weber number.

Head-on droplet collisions were simulated for a range of size ratios. Figure 11 shows the case of coalescence with $\Delta = 0.7$. For the following results the simulations used a fixed $R_s = 29$ and varied the size of the larger droplet. Figure 12 shows the results for the change in critical Weber number as the size ratio is varied. Again points represent boundaries between coalescence and separation (from varying U in intervals of 0.001 at fixed Δ, the plotted points being the midpoints between the two cases). Also shown is the theoretical result given in Eq. (33) at a fixed Ohnesorge number of Oh ≈ 0.04. The simulation results show slight errors from the theoretical prediction based on experimental results. While the simulation results tend to the theoretical results as the size ratio is increased, there is a larger error for nearly equal sized droplets. In the theoretical results critical Weber number decreases with decreasing $1/\Delta$, with the minimum $\mathrm{We_c}$ being at equal droplet size. The simulation results are in agreement with this trend initially, but show an increase in critical Weber number as $1/\Delta$ is decreased below approximately 1.4. The reason for this error in the LBM results is unclear, however some suggestions are now made. Again the low density ratio in the simulation could play a role. Increased gas pressure between the approaching droplets would slow both down in the near equal sized case, but would have less effect on the larger droplet as the size ratio decreased. Figure 12 shows the result for three different density ratios, and the result is seen to improve with increasing density ratio, as seen previously for equal sized droplets in Figure 9. However the highest density ratio is still below the experimental case, and the increased critical Weber number as the
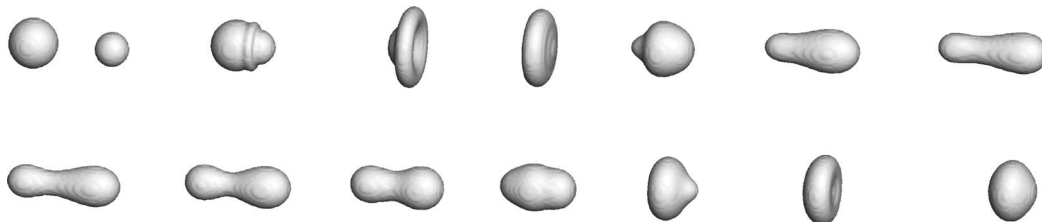

FIG. 11. Head-on coalescence of unequal sized droplets. We $= 49.7$, Re $= 179$, $\Delta = 0.7$.
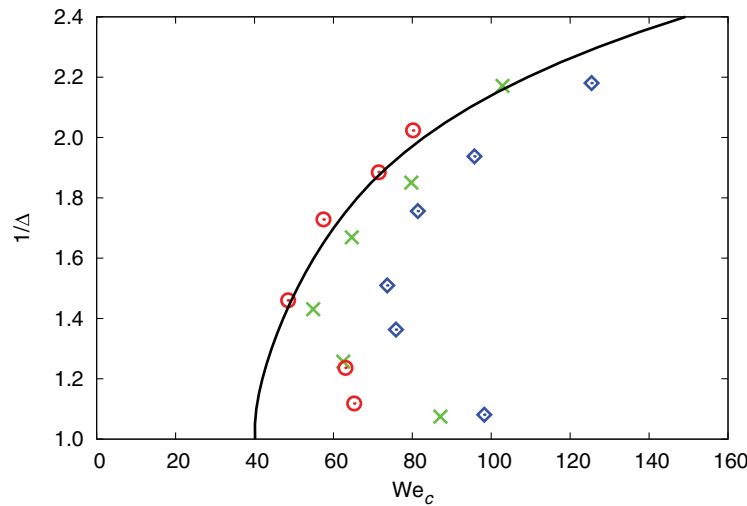
FIG. 12. The critical Weber number between head-on coalescence and separation, We_c, for varying inverse droplet size ratio, $1/\Delta$. Results are for density ratios of $\rho_r \approx 64$ (blue diamonds), $\rho_r \approx 128$ (green crosses), and $\rho_r \approx 256$ (red circles). The black line shows the theoretical prediction of Tang *et al.*[20]

droplets approach equal sizes is still observed. In the case of equal size droplets discussed above, density ratio was found to play a significant role, but could not alone explain the observed error. Other possible sources of error discussed in that case also apply here. Interestingly, Tang *et al.*[20] predicted a small increase in critical Weber number at equal droplet size, for certain viscosities, but did not show agreement with experiment (see Figure 10 of Ref. 20). Further work on this point would therefore be recommended.

3. Off-centre collisions

The agreement in linear trend and offset seen in Fig. 9 are a good indicator of the qualitative accuracy of the method, despite the higher gradient. We therefore proceed with a qualitative study of off-centre droplet collisions. For unequal size droplets Rabe *et al.*[19] proposed to define collisions by a symmetric Weber number, derived by correctly evaluating the ratio of kinetic to surface energies, as

$$We_s = \frac{\rho}{12\sigma} \frac{(2R_s)^3 U_s^2 + (2R_l)^3 U_l^2}{(2R_s)^2 + (2R_l)^2}. \tag{34}$$

Figure 13 shows results for collision outcomes of equal size droplets, for varying impact parameter and symmetric Weber number. Again points represent boundaries between coalescence and separation (from varying U in intervals of 0.002 at fixed B). By considering the relative importance of kinetic and surface energies, Rabe *et al.*[19] derived theoretical approximations for the boundaries between coalescence and near head-on separation, as

$$B_{c1} = B_\alpha \sqrt{1 - \frac{We_s^c}{We_s}}, \tag{35}$$

where B_α was measured experimentally as 0.28, and between coalescence and off-centre separation, as

$$B_{c2} = \frac{\sqrt{We_{st}^2 + 8We_{st}We_s} - We_{st}}{4We_s}, \tag{36}$$

where We_{st} is the "stretching Weber number," found experimentally to be 0.53. In Eq. (35) We_s^c is the critical point between head-on coalescence and separation for the symmetric Weber number, in the case of equal size droplets $We_s^c = We_c/48$. Rabe *et al.*[19] give $We_s^c = 0.45$ from experiment, however
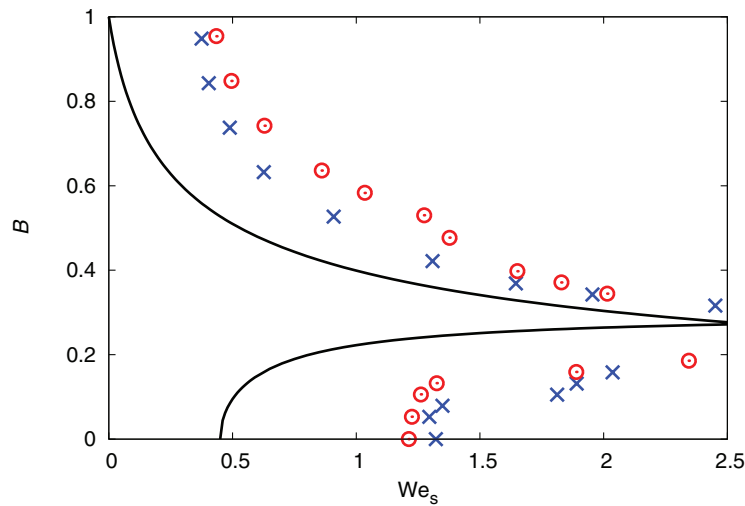
FIG. 13. Simulation results for transition between coalescence and separation for equal size droplets (blue cross) and unequal size droplets with $\Delta = 0.7$ (red circles). Black lines show the theoretical predictions given by Eqs. (35) and (36), using $We_s^c = 0.45$ as given by Rabe *et al.*[19]

critical Weber number should not be fixed (as shown in Fig. 9). $We_s^c = 0.45$ corresponds to the critical Weber number for equal sized droplets at $Oh \approx 0.01$. Rabe *et al.*[19] showed that Eq. (36) was in good agreement with experimental results, although data for $We_s < 0.25$ were not available, while Eq. (35) deviated slightly. These theoretical relationships are also plotted in Fig. 13. As discussed previously the critical Weber number between coalescence and separation for head-on collisions is too high in the present model, this also applies in the near head-on case. Figure 14 therefore shows the simulation results compared with Eq. (35), using the measured value of We_s^c from simulation, instead of $We_s^c = 0.45$. Using the measured value in the theoretical equation for the boundary allows comparison between the theoretical equation and the simulation results.
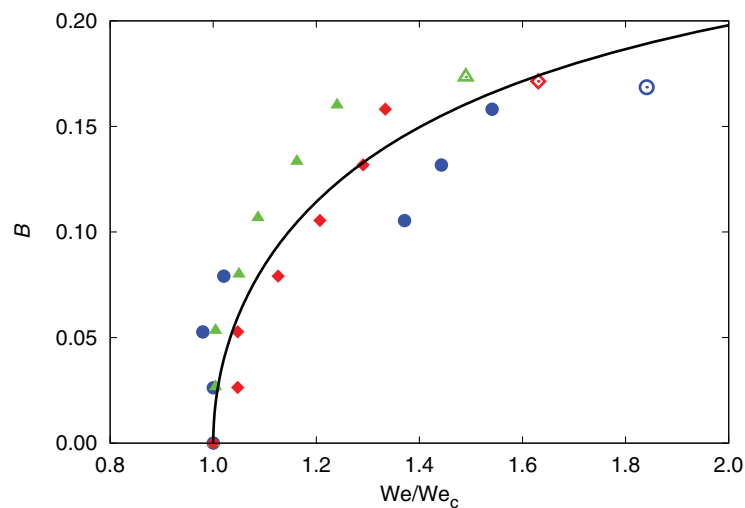
FIG. 14. Simulation results for transition between coalescence and near head-on separation for equal size droplets with viscosity $\nu = 0.0625$ (blue circles), $\nu = 0.0750$ (red diamonds), and $\nu = 0.0861$ (green triangles). Unfilled symbols indicate coalescence at the maximum simulated velocity. Weber number is normalised by the measured critical Weber number. The solid black line is the theoretical result from Rabe *et al.*,[19] given by Eq. (35), using the measured value of the critical Weber number from the simulation results.

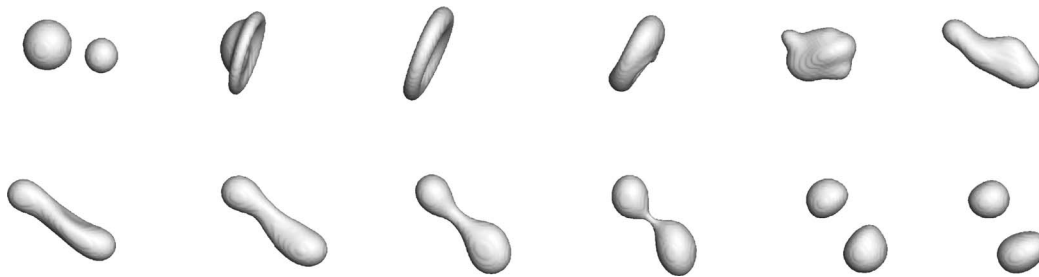FIG. 15. Near head-on separation of unequal sized droplets. We = 101, Re = 254, $\Delta = 0.7$, $B = 0.16$.

A number of observations can be made from Figs. 13 and 14. In general the LBM simulation results for both boundaries are seen to follow the shape of the predicted curves, however a number of differences are seen. For the boundary between coalescence and near head-on separation, at low impact parameter a slight initial decrease in Weber number is seen as B is increased that is not predicted by the theory. Some evidence for this can also be seen in the experimental results of Rabe *et al.*,[19] however further study is required for clarification. For the boundary between coalescence and off-centre separation, while the shape of the boundary is in agreement with the theory, it is found at a higher Weber number. Again this is likely to be due in part to the high gas pressure and other effects discussed above for the increased critical Weber number. However, the simulation result does not support the approach to We = 0 at $B = 1$. The diffusive interface plays a role in such glancing collisions, and as there is no experimental data at such low Weber numbers, again further work is required to clarify this point.

Although critical Weber number depends on viscosity, it can be seen from Eq. (35) that plotting (symmetric) Weber number normalised by critical (symmetric) Weber number against B is theoretically predicted to be independent of viscosity. Figure 14 shows the result given in Fig. 13 (for which $\nu = 0.0625$) normalised by critical Weber number, along with results for slightly higher viscosities of $\nu = 0.0750$ and $\nu = 0.0861$. The theoretical prediction of Eq. (35) is also shown, using the measured value of the critical Weber number from the simulation results. While in general good agreement is seen between the simulation results and the theoretical prediction, deviations are observed. First, the critical point is seen to increase with decreasing viscosity, especially as B approaches 0.2. This suggests that the constant B_α might be a function of viscosity. Droplet oscillations become more complex as B is increased, leading to increased viscous dissipation, an effect that was neglected in the theoretical prediction. However further investigation is required to clarify this point, especially as increasing liquid viscosity also increases gas viscosity in this model, as discussed previously. Second, the results do not all exactly follow the predicted smooth curve. Oscillations of the liquid bridge were observed to be a factor in the separation process in some simulations, the effect of which would not be captured by the theoretical predictions. Again further work is required to resolve this issue. Finally, no separation was observed above $B \approx 0.17$, which is slightly lower than the experimentally observed value.
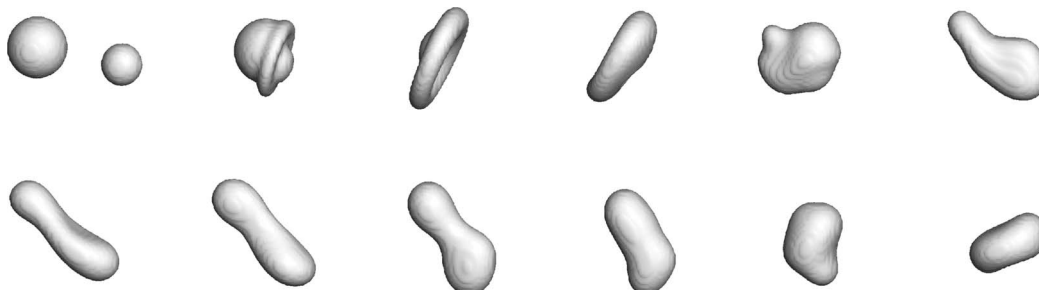

FIG. 16. Off-centre coalescence of unequal sized droplets. We = 66.3, Re = 206, $\Delta = 0.7$, $B = 0.21$.
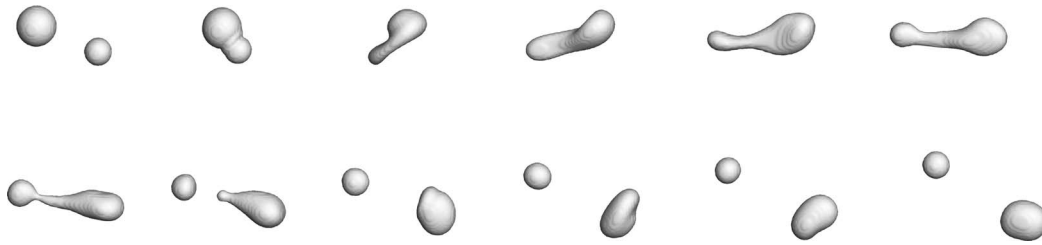
FIG. 17. Off-centre separation of unequal sized droplets. We $= 51.9$, Re $= 183$, $\Delta = 0.7$, $B = 0.64$.

For droplets of unequal size, Rabe *et al.*[19] found that the boundaries between collision regimes were independent of the size ratio, Δ, when using the symmetric Weber number. In deriving Eq. (35) they take viscous dissipation into account in a more simplified way than Tang *et al.*,[20] making it a constant coefficient fitted to their experimental data for water droplets. As discussed above, Tang *et al.*[20] showed that viscous dissipation in the second stage of a collision was dependent on size ratio. They also show that neglecting the dissipation in this stage resulted in predicting a critical Weber number almost independent of droplet size, which does not agree with experimental data. They argue that as the results presented by Rabe *et al.*[19] are for the low viscous case of water droplets, this effect is small. Additionally the lowest Δ presented is 0.5, and significant decrease in critical Weber number for water droplets is only predicted below this (Fig. 10 of Ref. 20). As Tang *et al.*[20] only discuss head-on collisions, it is still interesting to test the prediction of Rabe *et al.*[19] for off-centre collisions. As shown in Fig. 12, below $1/\Delta = 1.5$ only a slight increase in critical Weber number is predicted. Simulations were therefore conducted for droplets with $\Delta = 0.7$, the outcomes of which are given in Figs. 11, 15, 16, and 17 for head-on coalescence, near head-on separation, off-centre coalescence, and off-centre separation, respectively. The boundaries between collision regimes are also shown in Fig. 13. It can be seen that qualitatively there is some agreement with the findings of Rabe *et al.*,[19] with the regime boundaries for equal droplet sizes, and for $\Delta = 0.7$, lying close together. It is noted however that while the boundary between coalescence and near head-on separation is found at a slightly lower impact parameter for $\Delta = 0.7$, the boundary between coalescence and off-centre separation is found at a higher impact parameter. The reduction in critical Weber number of the simulation results at $\Delta = 0.7$ for the head-on case is shown in Fig. 12, and the accompanying discussion given above also applies to the near head-on collisions. The higher gas pressure would have less effect in the off-centre case, therefore the slight increase in critical Weber number at $\Delta = 0.7$ could come from similar viscous effects as discussed above in the head-on case.

V. CONCLUSION

A recently proposed application of the cascaded lattice Boltzmann method to multiphase flows[9] has been extended to three dimensions and applied to the case of binary droplet collisions. It has been shown that the cascaded LBM can significantly reduce spurious velocities around curved phase boundaries, and increase the range of attainable Reynolds numbers. This is achieved through tuning the additional relaxation parameters of the cascaded collision operator, and it has been shown that these parameters can be varied without significantly compromising the accuracy of the solution. Using this model it is possible to simulate droplet collisions at a density ratio of over 100, a Reynolds number of over 1000, and a Weber number of 100, simultaneously. With the exception of the density ratio being just one order of magnitude too low, this allows us to simulate droplet collisions under realistic experimental conditions.

This model has been extensively applied to binary droplet collisions, and simulation results for all droplet collision outcomes (up to a Weber number of 100 and with the exception of bouncing) have been obtained. A large number of simulations have been carried out to accurately determine the location of boundaries between different collision outcomes. In the case of head-on droplet collisions, the critical Weber number between separation and coalescence has been analysed. Good agreement with the experimental result of Qian and Law[17] for the relationship between Ohnesorge number

and critical Weber number was observed. The LBM results showed the correct linear relationship and offset from the origin, although over-predicted the gradient. This error in the LBM results was shown to be in part due to higher gas pressure, and critical Weber number was shown to decrease accordingly with decreasing gas pressure. Results for the variation in critical Weber number with droplet size ratio were compared with the theoretical predictions of Tang *et al.*[20] Good agreement was shown for unequal sized droplets, with the result again improving as gas pressure was reduced. The error in the LBM results compared with the theoretical prediction was found to decrease as the size ratio increased.

Rabe *et al.*[19] have recently developed theoretical boundaries between coalescence and separation based on a newly defined symmetric Weber number. Quantitative comparisons between the simulation results and the theoretical results showed general agreement, although a number of discrepancies are also reported. In the simulation results the boundary between coalescence and near head-on separation showed dependence on viscosity, which was neglected in the theoretical prediction. In the case of unequal size droplets the boundaries are predicted to coincide using the symmetric Weber number. Here, although the boundaries for a size ratio of $\Delta = 0.7$ were shown to be close to those of equal size droplets, differences were observed. Some improvements to the model are still required, which would allow further insight into different aspects of droplet collision phenomena. However, it has been shown that the multiphase cascaded LBM can offer valuable insight into this complex problem.

ACKNOWLEDGMENTS

APPENDIX A: RAW MOMENTS EXPRESSED IN TERMS OF CENTRAL MOMENTS

$$\Pi_{xy} = \tilde{\Pi}_{xy} + u_x u_y, \ \Pi_{xz} = \tilde{\Pi}_{xz} + u_x u_z, \ \Pi_{yz} = \tilde{\Pi}_{yz} + u_y u_z, \tag{A1}$$

$$N_{xz} = \tilde{N}_{xz} + (u_x^2 - u_z^2), \ N_{yz} = \tilde{N}_{yz} + (u_y^2 - u_z^2), \ T = \tilde{T} + u^2, \tag{A2}$$

$$Q_{xxy} = \tilde{Q}_{xxy} + 2u_x \tilde{\Pi}_{xy} + \frac{1}{3} u_y \tilde{T} + \frac{2}{3} u_y \tilde{N}_{xz} - \frac{1}{3} u_y \tilde{N}_{yz} + u_x^2 u_y, \tag{A3}$$

$$Q_{xxz} = \tilde{Q}_{xxz} + 2u_x \tilde{\Pi}_{xz} + \frac{1}{3} u_z \tilde{T} + \frac{2}{3} u_z \tilde{N}_{xz} - \frac{1}{3} u_z \tilde{N}_{yz} + u_x^2 u_z, \tag{A4}$$

$$Q_{xyy} = \tilde{Q}_{xyy} + 2u_y \tilde{\Pi}_{xy} + \frac{1}{3} u_x \tilde{T} - \frac{1}{3} u_x \tilde{N}_{xz} + \frac{2}{3} u_x \tilde{N}_{yz} + u_x u_y^2, \tag{A5}$$

$$Q_{yyz} = \tilde{Q}_{yyz} + 2u_y \tilde{\Pi}_{yz} + \frac{1}{3} u_z \tilde{T} - \frac{1}{3} u_z \tilde{N}_{xz} + \frac{2}{3} u_z \tilde{N}_{yz} + u_y^2 u_z, \tag{A6}$$

$$Q_{xzz} = \tilde{Q}_{xzz} + 2u_z \tilde{\Pi}_{xz} + \frac{1}{3} u_x \tilde{T} - \frac{1}{3} u_x \tilde{N}_{xz} - \frac{1}{3} u_x \tilde{N}_{yz} + u_x u_z^2, \tag{A7}$$

$$Q_{yzz} = \tilde{Q}_{yzz} + 2u_z \tilde{\Pi}_{yz} + \frac{1}{3} u_y \tilde{T} - \frac{2}{3} u_y \tilde{N}_{xz} - \frac{1}{3} u_y \tilde{N}_{yz} + u_y u_z^2, \tag{A8}$$

$$Q_{xyz} = \tilde{Q}_{xyz} + u_z \tilde{\Pi}_{xy} + u_y \tilde{\Pi}_{xz} + u_x \tilde{\Pi}_{yz} + u_x u_y u_z, \tag{A9}$$

$$A_{xxyy} = \tilde{A}_{xxyy} + 2u_y\tilde{Q}_{xxy} + 2u_x\tilde{Q}_{xyy} + 4u_xu_y\tilde{\Pi}_{xy} + \frac{1}{3}\left(u_x^2 + u_y^2\right)\tilde{T}$$
$$+ \left(-\frac{1}{3}u_x^2 + \frac{2}{3}u_y^2\right)\tilde{N}_{xz} + \left(\frac{2}{3}u_x^2 - \frac{1}{3}u_y^2\right)\tilde{N}_{yz} + u_x^2u_y^2, \tag{A10}$$

$$A_{xxzz} = \tilde{A}_{xxzz} + 2u_z\tilde{Q}_{xxz} + 2u_x\tilde{Q}_{xzz} + 4u_xu_z\tilde{\Pi}_{xz} + \frac{1}{3}\left(u_x^2 + u_z^2\right)\tilde{T}$$
$$+ \left(-\frac{1}{3}u_x^2 + \frac{2}{3}u_z^2\right)\tilde{N}_{xz} + \left(-\frac{1}{3}u_x^2 - \frac{1}{3}u_z^2\right)\tilde{N}_{yz} + u_x^2u_z^2, \tag{A11}$$

$$A_{yyzz} = \tilde{A}_{yyzz} + 2u_z\tilde{Q}_{yyz} + 2u_y\tilde{Q}_{yzz} + 4u_yu_z\tilde{\Pi}_{yz} + \frac{1}{3}\left(u_y^2 + u_z^2\right)\tilde{T}$$
$$+ \left(-\frac{1}{3}u_y^2 - \frac{1}{3}u_z^2\right)\tilde{N}_{xz} + \left(-\frac{1}{3}u_y^2 + \frac{2}{3}u_z^2\right)\tilde{N}_{yz} + u_y^2u_z^2, \tag{A12}$$

$$M_{211} = \tilde{M}_{211} + u_z\tilde{Q}_{xxy} + u_y\tilde{Q}_{xxz} + 2u_x\tilde{Q}_{xyz} + 2u_xu_z\tilde{\Pi}_{xy} + 2u_xu_y\tilde{\Pi}_{xz} + 2u_x^2\tilde{\Pi}_{yz}$$
$$+ \frac{1}{3}u_yu_z\tilde{T} + \frac{2}{3}u_yu_z\tilde{N}_{xz} - \frac{1}{3}u_yu_z\tilde{N}_{yz} + u_x^2u_yu_z, \tag{A13}$$

$$M_{121} = \tilde{M}_{121} + u_z\tilde{Q}_{xyy} + u_x\tilde{Q}_{yyz} + 2u_y\tilde{Q}_{xyz} + 2u_yu_z\tilde{\Pi}_{xy} + u_y^2\tilde{\Pi}_{xz} + 2u_xu_y\tilde{\Pi}_{yz}$$
$$+ \frac{1}{3}u_xu_z\tilde{T} - \frac{1}{3}u_xu_z\tilde{N}_{xz} + \frac{2}{3}u_xu_z\tilde{N}_{yz} + u_xu_y^2u_z, \tag{A14}$$

$$M_{112} = \tilde{M}_{112} + u_y\tilde{Q}_{xzz} + u_x\tilde{Q}_{yzz} + 2u_z\tilde{Q}_{xyz} + u_z^2\tilde{\Pi}_{xy} + 2u_yu_z\tilde{\Pi}_{xz} + 2u_xu_z\tilde{\Pi}_{yz}$$
$$+ \frac{1}{3}u_xu_y\tilde{T} - \frac{1}{3}u_xu_y\tilde{N}_{xz} - \frac{1}{3}u_xu_y\tilde{N}_{yz} + u_xu_yu_z^2, \tag{A15}$$

$$M_{221} = \tilde{M}_{221} + 2u_y\tilde{M}_{211} + 2u_x\tilde{M}_{121} + u_z\tilde{A}_{xxyy}$$
$$+ 2u_yu_z\tilde{Q}_{xxy} + u_y^2\tilde{Q}_{xxz} + 2u_xu_z\tilde{Q}_{xyy} + u_x^2\tilde{Q}_{yyz} + 4u_xu_y\tilde{Q}_{xyz}$$
$$+ 4u_xu_yu_z\tilde{\Pi}_{xy} + 2u_xu_y^2\tilde{\Pi}_{xz} + 2u_x^2u_y\tilde{\Pi}_{yz} + \frac{1}{3}\left(u_x^2u_z + u_y^2u_z\right)\tilde{T}$$
$$+ \left(-\frac{1}{3}u_x^2u_z + \frac{2}{3}u_y^2u_z\right)\tilde{N}_{xz} + \left(\frac{2}{3}u_x^2u_z - \frac{1}{3}u_y^2u_z\right)\tilde{N}_{yz} + u_x^2u_y^2u_z, \tag{A16}$$

$$M_{212} = \tilde{M}_{212} + 2u_z\tilde{M}_{211} + 2u_x\tilde{M}_{112} + u_y\tilde{A}_{xxzz}$$
$$+ u_z^2\tilde{Q}_{xxy} + 2u_yu_z\tilde{Q}_{xxz} + 2u_xu_y\tilde{Q}_{xzz} + u_x^2\tilde{Q}_{yzz} + 4u_xu_z\tilde{Q}_{xyz}$$
$$+ 2u_xu_z^2\tilde{\Pi}_{xy} + 4u_xu_yu_z\tilde{\Pi}_{xz} + 2u_x^2u_z\tilde{\Pi}_{yz} + \frac{1}{3}\left(u_x^2u_y + u_yu_z^2\right)\tilde{T}$$
$$+ \left(-\frac{1}{3}u_x^2u_y + \frac{2}{3}u_yu_z^2\right)\tilde{N}_{xz} + \left(-\frac{1}{3}u_x^2u_y - \frac{1}{3}u_yu_z^2\right)\tilde{N}_{yz} + u_x^2u_yu_z^2, \tag{A17}$$

$$M_{122} = \tilde{M}_{122} + 2u_z\tilde{M}_{121} + 2u_y\tilde{M}_{112} + u_x\tilde{A}_{yyzz}$$
$$+ u_z^2\tilde{Q}_{xyy} + 2u_xu_z\tilde{Q}_{yyz} + u_y^2\tilde{Q}_{xzz} + 2u_xu_y\tilde{Q}_{yzz} + 4u_yu_z\tilde{Q}_{xyz}$$
$$+ 2u_yu_z^2\tilde{\Pi}_{xy} + 2u_y^2u_z\tilde{\Pi}_{xz} + 4u_xu_yu_z\tilde{\Pi}_{yz} + \frac{1}{3}\left(u_xu_y^2 + u_xu_z^2\right)\tilde{T}$$
$$+ \left(-\frac{1}{3}u_xu_y^2 - \frac{1}{3}u_xu_z^2\right)\tilde{N}_{xz} + \left(-\frac{1}{3}u_xu_y^2 + \frac{2}{3}u_xu_z^2\right)\tilde{N}_{yz} + u_xu_y^2u_z^2, \qquad \text{(A18)}$$

$$M_{222} = \tilde{M}_{222} + 2u_z\tilde{M}_{221} + 2u_y\tilde{M}_{212} + 2u_x\tilde{M}_{122}$$
$$+ 4u_yu_z\tilde{M}_{211} + 4u_xu_z\tilde{M}_{121} + 4u_xu_y\tilde{M}_{112} + u_z^2\tilde{A}_{xxyy} + u_y^2\tilde{A}_{xxzz} + u_x^2\tilde{A}_{yyzz}$$
$$+ 2u_yu_z^2\tilde{Q}_{xxy} + 2u_y^2u_z\tilde{Q}_{xxz} + 2u_xu_z^2\tilde{Q}_{xyy}$$
$$+ 2u_x^2u_z\tilde{Q}_{yyz} + 2u_xu_y^2\tilde{Q}_{xzz} + 2u_x^2u_y\tilde{Q}_{yzz} + 8u_xu_yu_z\tilde{Q}_{xyz}$$
$$+ 4u_xu_yu_z^2\tilde{\Pi}_{xy} + 4u_xu_y^2u_z\tilde{\Pi}_{xz} + 4u_x^2u_yu_z\tilde{\Pi}_{yz}$$
$$+ \left(-\frac{1}{3}u_x^2u_y^2 - \frac{1}{3}u_x^2u_z^2 + \frac{2}{3}u_y^2u_z^2\right)\tilde{N}_{xz} + \left(-\frac{1}{3}u_x^2u_y^2 + \frac{2}{3}u_x^2u_z^2 - \frac{1}{3}u_y^2u_z^2\right)\tilde{N}_{yz}$$
$$+ \frac{1}{3}\left(u_x^2u_y^2 + u_x^2u_z^2 + u_y^2u_z^2\right)\tilde{T} + u_x^2u_y^2u_z^2. \qquad \text{(A19)}$$

APPENDIX B: POST-COLLISION DISTRIBUTIONS

$$f^*_{(\sigma,0,0)} = \frac{\rho}{2}\Bigg[\frac{1}{27} + u_x^2 + \sigma u_x\left(1 - u_y^2 - u_z^2\right) + \left(-4u_xu_y + 2\sigma u_y(u_z^2 - 1)\right)\tilde{\Pi}^*_{xy}$$
$$+ \left(-4u_xu_z + 2\sigma u_z(u_y^2 - 1)\right)\tilde{\Pi}^*_{xz} + 4\sigma u_xu_yu_z\tilde{\Pi}^*_{yz}$$
$$+ \frac{1}{3}\left(2(1 + u_x^2 - u_y^2 - u_z^2) + \sigma u_x(2 - u_y^2 - u_z^2)\right)\tilde{N}^*_{xz}$$
$$+ \frac{1}{3}\left(-1 - u_x^2 + u_y^2 + u_z^2 + \sigma u_x(-1 - u_y^2 + 2u_z^2)\right)\tilde{N}^*_{yz}$$
$$+ \frac{1}{3}\left(1 - 2u_x^2 - u_y^2 - u_z^2 + \sigma u_x(-2 + u_y^2 + u_z^2)\right)\tilde{T}^*$$
$$+ 2u_y\left(u_z^2 - 1\right)\tilde{Q}^*_{xxy} + 2u_z\left(u_y^2 - 1\right)\tilde{Q}^*_{xxz} + (\sigma + 2u_x)\left(u_z^2 - 1\right)\tilde{Q}^*_{xyy}$$
$$+ 2u_xu_z\left(\sigma + u_x\right)\tilde{Q}^*_{yyz} + (\sigma + 2u_x)\left(u_y^2 - 1\right)\tilde{Q}^*_{xzz} + 2u_xu_y\left(\sigma + u_x\right)\tilde{Q}^*_{yzz}$$
$$+ \left(u_z^2 - 1\right)\tilde{A}^*_{xxyy} + \left(u_y^2 - 1\right)\tilde{A}^*_{xxzz} + \left(u_x^2 + \sigma u_x\right)\tilde{A}^*_{yyzz}\Bigg], \qquad \text{(B1)}$$

$$f^*_{(0,\lambda,0)} = \frac{\rho}{2}\Bigg[\frac{1}{27} + u_y^2 + \lambda u_y\left(1 - u_x^2 - u_z^2\right) + \left(-4u_xu_y + 2\lambda u_x(u_z^2 - 1)\right)\tilde{\Pi}^*_{xy}$$
$$+ 4\lambda u_xu_yu_z\tilde{\Pi}^*_{xz} + \left(-4u_yu_z + 2\lambda u_z(u_x^2 - 1)\right)\tilde{\Pi}^*_{yz}$$
$$+ \frac{1}{3}\left(-1 + u_x^2 - u_y^2 + u_z^2 + \lambda u_y(-1 - u_x^2 + 2u_z^2)\right)\tilde{N}^*_{xz}$$
$$+ \frac{1}{3}\left(2(1 - u_x^2 + u_y^2 - u_z^2) + \lambda u_y(2 - u_x^2 - u_z^2)\right)\tilde{N}^*_{yz}$$

$$+ \frac{1}{3} \left(1 - u_x^2 - 2u_y^2 - u_z^2 + \lambda u_y(-2 + u_x^2 + u_z^2)\right) \tilde{T}^*$$

$$+ (\lambda + 2u_y)\left(u_z^2 - 1\right) \tilde{Q}_{xxy}^* + 2u_y u_z \left(\lambda + u_y\right) \tilde{Q}_{xxz}^* + 2u_x \left(u_z^2 - 1\right) \tilde{Q}_{xyy}^*$$

$$+ 2u_z \left(u_x^2 - 1\right) \tilde{Q}_{yyz}^* + 2u_x u_y \left(\lambda + u_y\right) \tilde{Q}_{xzz}^* + (\lambda + 2u_y)\left(u_x^2 - 1\right) \tilde{Q}_{yzz}^*$$

$$+ \left(u_z^2 - 1\right) \tilde{A}_{xxyy}^* + \left(u_y^2 + \lambda u_y\right) \tilde{A}_{xxzz}^* + \left(u_x^2 - 1\right) \tilde{A}_{yyzz}^* \Bigg], \tag{B2}$$

$$f_{(0,0,\delta)}^* = \frac{\rho}{2}\Bigg[\frac{1}{27} + u_z^2 + \delta u_z \left(1 - u_x^2 - u_y^2\right) + 4\delta u_x u_y u_z \tilde{\Pi}_{xy}^*$$

$$+ \left(-4u_x u_z + 2\delta u_x(u_y^2 - 1)\right) \tilde{\Pi}_{xz}^* + \left(-4u_y u_z + 2\delta u_y(u_x^2 - 1)\right) \tilde{\Pi}_{yz}^*$$

$$+ \frac{1}{3}\left(-1 + u_x^2 + u_y^2 - u_z^2 + \delta u_z(-1 - u_x^2 + 2u_y^2)\right) \tilde{N}_{xz}^*$$

$$+ \frac{1}{3}\left(-1 + u_x^2 + u_y^2 - u_z^2 + \delta u_z(-1 + 2u_x^2 - u_y^2)\right) \tilde{N}_{yz}^*$$

$$+ \frac{1}{3}\left(1 - u_x^2 - u_y^2 - 2u_z^2 + \delta u_z(-2 + u_x^2 + u_y^2)\right) \tilde{T}^*$$

$$+ 2u_y u_z \left(\delta + u_z\right) \tilde{Q}_{xxy}^* + (\delta + 2u_z)\left(u_y^2 - 1\right) \tilde{Q}_{xxz}^* + 2u_x u_z \left(\delta + u_z\right) \tilde{Q}_{xyy}^*$$

$$+ (\delta + 2u_z)\left(u_x^2 - 1\right) \tilde{Q}_{yyz}^* + 2u_x \left(u_y^2 - 1\right) \tilde{Q}_{xzz}^* + 2u_y \left(u_x^2 - 1\right) \tilde{Q}_{yzz}^*$$

$$+ \left(u_z^2 + \delta u_z\right) \tilde{A}_{xxyy}^* + \left(u_y^2 - 1\right) \tilde{A}_{xxzz}^* + \left(u_x^2 - 1\right) \tilde{A}_{yyzz}^* \Bigg], \tag{B3}$$

$$f_{(\sigma,\lambda,0)}^* = \frac{\rho}{4}\Bigg[-\frac{1}{27} + \sigma\lambda u_x u_y + \lambda u_x^2 u_y + \sigma u_x u_y^2$$

$$+ \left(4u_x u_y + 2(\lambda u_x + \sigma u_y)(1 - u_z^2) - \sigma\lambda u_z^2\right) \tilde{\Pi}_{xy}^*$$

$$- u_y u_z \left(2\sigma\lambda + 4\lambda u_x + 2\sigma u_y\right) \tilde{\Pi}_{xz}^* - u_x u_z \left(2\sigma\lambda + 2\lambda u_x + 4\sigma u_y\right) \tilde{\Pi}_{yz}^*$$

$$+ \frac{1}{3}\big(-\sigma u_x + 2\lambda u_y - u_x^2 + 2u_y^2 + \sigma\lambda u_x u_y$$

$$+ \lambda u_x^2 u_y + \sigma u_x u_y^2 + \sigma u_x u_z^2 - 2\lambda u_y u_z^2 \big) \tilde{N}_{xz}^*$$

$$+ \frac{1}{3}\big(2\sigma u_x - \lambda u_y + 2u_x^2 - u_y^2 + \sigma\lambda u_x u_y$$

$$+ \lambda u_x^2 u_y + \sigma u_x u_y^2 - 2\sigma u_x u_z^2 + \lambda u_y u_z^2 \big) \tilde{N}_{yz}^*$$

$$+ \frac{1}{3}\big(\sigma u_x + \lambda u_y + u_x^2 + u_y^2 - \sigma\lambda u_x u_y$$

$$- \lambda u_x^2 u_y - \sigma u_x u_y^2 - \sigma u_x u_z^2 - \lambda u_y u_z^2 \big) \tilde{T}^*$$

$$+ (\lambda + 2u_y)\left(1 - u_z^2\right) \tilde{Q}_{xxy}^* - 2u_y u_z \left(\lambda + u_y\right) \tilde{Q}_{xxz}^*$$

$$+ (\sigma + 2u_x)\left(1 - u_z^2\right) \tilde{Q}_{xyy}^* - 2u_x u_z \left(\sigma + u_x\right) \tilde{Q}_{yyz}^*$$

$$- (\sigma + 2u_x)\left(\lambda u_y + u_y^2\right) \tilde{Q}_{xzz}^* - (\lambda + 2u_y)\left(\sigma u_x + u_x^2\right) \tilde{Q}_{yzz}^*$$

$$+ \left(1 - u_z^2\right) \tilde{A}_{xxyy}^* - \left(\lambda u_y + u_y^2\right) \tilde{A}_{xxzz}^* - \left(\sigma u_x + u_x^2\right) \tilde{A}_{yyzz}^* \Bigg], \tag{B4}$$

$$
\begin{aligned}
f_{(\sigma,0,\delta)}^{*} = \frac{\rho}{4}\bigg[&-\frac{1}{27} + \sigma\delta u_x u_z + \delta u_x^2 u_z + \sigma u_x u_z^2 \\
&+ \left(2\delta u_x + 2\sigma u_z - \sigma\delta u_y^2 + 4u_x u_z - 2\delta u_x u_y^2 - 2\sigma u_y^2 u_z\right)\tilde{\Pi}_{xz}^{*} \\
&- u_y u_z \left(2\sigma\delta + 4\delta u_x + 2\sigma u_z\right)\tilde{\Pi}_{xy}^{*} - u_x u_y \left(2\sigma\delta + 2\delta u_x + 4\sigma u_z\right)\tilde{\Pi}_{yz}^{*} \\
&+ \frac{1}{3}\big(-\sigma u_x + 2\delta u_z - u_x^2 + 2u_z^2 + \sigma\delta u_x u_z \\
&+ \delta u_x^2 u_z + \sigma u_x u_y^2 + \sigma u_x u_z^2 - 2\delta u_y^2 u_z\big)\tilde{N}_{xz}^{*} \\
&+ \frac{1}{3}\big(-\sigma u_x - \delta u_z - u_x^2 - u_z^2 - 2\sigma\delta u_x u_z \\
&- 2\delta u_x^2 u_z + \sigma u_x u_y^2 - 2\sigma u_x u_z^2 + \delta u_y^2 u_z\big)\tilde{N}_{yz}^{*} \\
&+ \frac{1}{3}\big(\sigma u_x + \delta u_z + u_x^2 + u_z^2 - \sigma\delta u_x u_z \\
&- \delta u_x^2 u_z - \sigma u_x u_y^2 - \sigma u_x u_z^2 - \delta u_y^2 u_z\big)\tilde{T}^{*} \\
&- 2u_y u_z \left(\delta + u_z\right)\tilde{Q}_{xxy}^{*} + \left(\delta + 2u_z\right)\left(1 - u_y^2\right)\tilde{Q}_{xxz}^{*} \\
&- \left(\sigma + 2u_x\right)\left(\delta u_z + u_z^2\right)\tilde{Q}_{xyy}^{*} - \left(\delta + 2u_z\right)\left(\sigma u_x + u_x^2\right)\tilde{Q}_{yyz}^{*} \\
&+ \left(\sigma + 2u_x\right)\left(1 - u_y^2\right)\tilde{Q}_{xzz}^{*} - 2u_x u_y \left(\sigma + u_x\right)\tilde{Q}_{yzz}^{*} \\
&- \left(\delta u_z + u_z^2\right)\tilde{A}_{xxyy}^{*} + \left(1 - u_y^2\right)\tilde{A}_{xxzz}^{*} - \left(\sigma u_x + u_x^2\right)\tilde{A}_{yyzz}^{*}\bigg],
\end{aligned}
\tag{B5}
$$

$$
\begin{aligned}
f_{(0,\lambda,\delta)}^{*} = \frac{\rho}{4}\bigg[&-\frac{1}{27} + \lambda\delta u_y u_z + \delta u_y^2 u_z + \lambda u_y u_z^2 \\
&+ \left(2\delta u_y + 2\lambda u_z - \lambda\delta u_x^2 + 4u_y u_z - 2\delta u_x^2 u_y - 2\lambda u_x^2 u_z\right)\tilde{\Pi}_{yz}^{*} \\
&- u_x u_z \left(2\lambda\delta + 4\delta u_y + 2\lambda u_z\right)\tilde{\Pi}_{xy}^{*} - u_x u_y \left(2\lambda\delta + 2\delta u_y + 4\lambda u_z\right)\tilde{\Pi}_{xz}^{*} \\
&+ \frac{1}{3}\big(-\lambda u_y - \delta u_z - u_y^2 - u_z^2 - 2\lambda\delta u_y u_z \\
&+ \lambda u_x^2 u_y + \delta u_x^2 u_z - 2\delta u_y^2 u_z - 2\lambda u_y u_z^2\big)\tilde{N}_{xz}^{*} \\
&+ \frac{1}{3}\big(-\lambda u_y + 2\delta u_z - u_y^2 + 2u_z^2 + \lambda\delta u_y u_z \\
&+ \lambda u_x^2 u_y - 2\delta u_x^2 u_z + \delta u_y^2 u_z + \lambda u_y u_z^2\big)\tilde{N}_{yz}^{*} \\
&+ \frac{1}{3}\big(\lambda u_y + \delta u_z + u_y^2 + u_z^2 - \lambda\delta u_y u_z \\
&- \lambda u_x^2 u_y - \delta u_x^2 u_z - \delta u_y^2 u_z - \lambda u_y u_z^2\big)\tilde{T}^{*} \\
&- \left(\lambda + 2u_y\right)\left(\delta u_z + u_z^2\right)\tilde{Q}_{xxy}^{*} - \left(\delta + 2u_z\right)\left(\lambda u_y + u_y^2\right)\tilde{Q}_{xxz}^{*} \\
&- 2u_x u_z \left(\delta + u_z\right)\tilde{Q}_{xyy}^{*} + \left(\delta + 2u_z\right)\left(1 - u_x^2\right)\tilde{Q}_{yyz}^{*} \\
&- 2u_x u_y \left(\lambda + u_y\right)\tilde{Q}_{xzz}^{*} + \left(\lambda + 2u_y\right)\left(1 - u_x^2\right)\tilde{Q}_{yzz}^{*} \\
&- \left(\delta u_z + u_z^2\right)\tilde{A}_{xxyy}^{*} - \left(\lambda u_y + u_y^2\right)\tilde{A}_{xxzz}^{*} + \left(1 - u_x^2\right)\tilde{A}_{yyzz}^{*}\bigg],
\end{aligned}
\tag{B6}
$$

$$
\begin{aligned}
f^*_{(\sigma,\lambda,\delta)} = \frac{\rho}{8}\Bigg[& \frac{1}{27} + \sigma\lambda\delta u_x u_y u_z \\
& + \big(\sigma\lambda u_z^2 + 2\lambda\delta u_x u_z + 2\sigma\delta u_y u_z + 2\lambda u_x u_z^2 + 2\sigma u_y u_z^2 + 4\delta u_x u_y u_z\big)\tilde{\Pi}^*_{xy} \\
& + \big(\sigma\delta u_y^2 + 2\lambda\delta u_x u_y + 2\sigma\lambda u_y u_z + 2\delta u_x u_y^2 + 2\sigma u_y^2 u_z + 4\lambda u_x u_y u_z\big)\tilde{\Pi}^*_{xz} \\
& + \big(\lambda\delta u_x^2 + 2\sigma\delta u_x u_y + 2\sigma\lambda u_x u_z + 2\delta u_x^2 u_y + 2\lambda u_x^2 u_z + 4\sigma u_x u_y u_z\big)\tilde{\Pi}^*_{yz} \\
& + \frac{1}{3}\big(-\sigma\lambda u_x u_y - \sigma\delta u_x u_z + 2\lambda\delta u_y u_z - \lambda u_x^2 u_y \\
& \quad - \delta u_x^2 u_z - \sigma u_x u_y^2 + 2\delta u_y^2 u_z - \sigma u_x u_z^2 + 2\lambda u_y u_z^2\big)\tilde{N}^*_{xz} \\
& + \frac{1}{3}\big(-\sigma\lambda u_x u_y + 2\sigma\delta u_x u_z - \lambda\delta u_y u_z - \lambda u_x^2 u_y \\
& \quad + 2\delta u_x^2 u_z - \sigma u_x u_y^2 - \delta u_y^2 u_z + 2\sigma u_x u_z^2 - \lambda u_y u_z^2\big)\tilde{N}^*_{yz} \\
& + \frac{1}{3}\big(\sigma\lambda u_x u_y + \sigma\delta u_x u_z + \lambda\delta u_y u_z + \lambda u_x^2 u_y \\
& \quad + \delta u_x^2 u_z + \sigma u_x u_y^2 + \delta u_y^2 u_z + \sigma u_x u_z^2 + \lambda u_y u_z^2\big)\tilde{T}^* \\
& + \big(\lambda + 2u_y\big)\big(\delta u_z + u_z^2\big)\tilde{Q}^*_{xxy} + \big(\delta + 2u_z\big)\big(\lambda u_y + u_y^2\big)\tilde{Q}^*_{xxz} \\
& + \big(\sigma + 2u_x\big)\big(\delta u_z + u_z^2\big)\tilde{Q}^*_{xyy} + \big(\delta + 2u_z\big)\big(\sigma u_x + u_x^2\big)\tilde{Q}^*_{yyz} \\
& + \big(\sigma + 2u_x\big)\big(\lambda u_y + u_y^2\big)\tilde{Q}^*_{xzz} + \big(\lambda + 2u_y\big)\big(\sigma u_x + u_x^2\big)\tilde{Q}^*_{yzz} \\
& + \big(\delta u_z + u_z^2\big)\tilde{A}^*_{xxyy} + \big(\lambda u_y + u_y^2\big)\tilde{A}^*_{xxzz} + \big(\sigma u_x + u_x^2\big)\tilde{A}^*_{yyzz} \Bigg].
\end{aligned}
\tag{B7}
$$

[1] S. Chen and G. D. Doolen, "Lattice Boltzmann method for fluid flows," Annu. Rev. Fluid Mech. **30**, 329 (1998).

[2] Y. H. Qian, S. Succi, and S. A. Orszag, "Recent advances in lattice Boltzmann computing," Annu. Rev. Comput. Phys. **30**, 195 (1995).

[3] S. Succi, *The Lattice Boltzmann Equation for Fluid Dynamics and Beyond* (Oxford University Press, Oxford, 2001).

[4] D. d'Humières, "Generalized lattice-Boltzmann equations" in *Rarefied Gas Dynamics: Theory and Simulations, Progress in Astronautics and Aeronautics*, edited by B. D. Shizgal and D. P. Weaver (AIAA Press, Washington, DC, 1992), Vol. 159, p. 450.

[5] D. d'Humières, I. Ginzburg, M. Krafczyk, P. Lallemand, and L.-S. Luo, "Multiple-relaxation-time lattice Boltzmann models in three dimensions," Philos. Trans. R. Soc. London, A **360**, 437 (2002).

[6] P. Lallemand and L.-S. Luo, "Theory of the lattice Boltzmann method: Dispersion, dissipation, isotropy, Galilean invariance, and stability," Phys. Rev. E **61**, 6546 (2000).

[7] P. Lallemand and L.-S. Luo, "Theory of the lattice Boltzmann method: Acoustic and thermal properties in two and three dimensions," Phys. Rev. E **68**, 036706 (2003).

[8] M. C. Geier, A. Greiner, and J. G. Korvink, "Cascaded digital lattice Boltzmann automata for high Reynolds number flow," Phys. Rev. E **73**, 066705 (2006).

[9] D. Lycett-Brown and K. H. Luo, "Multiphase cascaded lattice Boltzmann method," Comput. Math. Appl. **67**, 350 (2014).

[10] X. Shan and H. Chen, "Lattice Boltzmann model for simulating flows with multiple phases and components," Phys. Rev. E **47**, 1815 (1993).

[11] X. Shan and H. Chen, "Simulation of nonideal gases and liquid-gas phase transitions by the lattice Boltzmann equation," Phys. Rev. E **49**, 2941 (1994).

[12] A. L. Kupershtokh, D. A. Medvedev, and D. I. Karpov, "On equations of state in a lattice Boltzmann method," Comput. Math. Appl. **58**, 965 (2009).

[13] B. F. Lin, J. H. Huang, and D. Y. Huang, "Experimental study of the effects of vegetable oil methyl ester on DI diesel engine performance characteristics and pollutant emissions," Fuel **88**, 1779 (2009).

[14] C. Öner and S. Altun, "Biodiesel production from inedible animal tallow and an experimental investigation of its use as alternative fuel in a direct injection diesel engine," Appl. Energy **86**, 2114 (2009).

[15] H. Aydin and H. Bayindir, "Performance and emission analysis of cottonseed oil methyl ester in a diesel engine," Renewable Energy **35**, 588 (2010).

[16] Z. Utlua and M. S. Koçak, "The effect of biodiesel fuel obtained from waste frying oil on direct injection diesel engine performance and exhaust emissions," Renewable Energy **33**, 1936 (2008).

[17] J. Qian and C. K. Law, "Regimes of coalescence and separation in droplet collision," J. Fluid Mech. **331**, 59 (1997).

[18] N. Ashgriz and J. Y. Poo, "Coalescence and separation in binary collisions of liquid drops," J. Fluid Mech. **221**, 183 (1990).

[19] C. Rabe, J. Malet, and F. Feuillebois, "Experimental investigation of water droplet binary collisions and description of outcomes with a symmetric Weber number," Phys. Fluids **22**, 047101 (2010).

[20] C. Tang, P. Zhang, and C. K. Law, "Bouncing, coalescence, and separation in head-on collision of unequal-size droplets," Phys. Fluids **24**, 022101 (2012).

[21] K.-L. Pan, P.-C. Chou, and Y.-J. Tseng, "Binary droplet collision at high Weber number," Phys. Rev. E **80**, 036301 (2009).

[22] Y. Pan and K. Suga, "Numerical simulation of binary liquid droplet collision," Phys. Fluids **17**, 082105 (2005).

[23] S. Tanguy and A. Berlemont, "Application of a level set method for simulation of droplet collisions," Int. J. Multiphase Flow **31**, 1015 (2005).

[24] N. Nikolopoulos and G. Bergeles, "The effect of gas and liquid properties and droplet size ratio on the central collision between two unequal-size droplets in the reflexive regime," Int. J. Heat Mass Transfer **54**, 678 (2011).

[25] T. Inamuro, S. Tajima, and F. Ogino, "Lattice Boltzmann simulation of droplet collision dynamics," Int. J. Heat Mass Transfer **47**, 4649 (2004).

[26] K. H. Luo, J. Xia, and E. Monaco, "Multiscale modeling of multiphase flow with complex interactions," J. Multiscale Modell. **01**, 125 (2009).

[27] C. Focke and D. Bothe, "Direct numerical simulation of binary off-centre collisions of shear thinning droplets at high Weber numbers," Phys. Fluids **24**, 073105 (2012).

[28] I. V. Karlin and P. Asinari, "Factorization symmetry in the lattice Boltzmann method," Physica A **389**, 1530 (2010).

[29] M. C. Geier, A. Greiner, and J. G. Korvink, "Properties of the cascaded lattice Boltzmann automaton," Int. J. Mod. Phys. C **18**, 455 (2007).

[30] E. Orlandini, M. R. Swift, and J. M. Yeomans, "A lattice Boltzmann model of binary-fluid mixtures," Europhys. Lett. **32**, 463 (1995).

[31] M. R. Swift, E. Orlandini, W. R. Osborn, and J. M. Yeomans, "Lattice Boltzmann simulations of liquid-gas and binary fluid systems," Phys. Rev. E **54**, 5041 (1996).

[32] M. R. Swift, W. R. Osborn, and J. M. Yeomans, "Lattice Boltzmann simulation of nonideal fluids," Phys. Rev. Lett. **75**, 830 (1995).

[33] X. He and G. D. Doolen, "Thermodynamic foundations of kinetic theory and lattice Boltzmann models for multiphase flows," J. Stat. Phys. **107**, 309 (2002).

[34] X. He, X. Shan, and G. D. Doolen, "Discrete Boltzmann equation model for nonideal gases," Phys. Rev. E **57**, R13 (1998).

[35] L.-S. Luo, "Unified theory of lattice Boltzmann models for nonideal gases," Phys. Rev. Lett. **81**, 1618 (1998).

[36] X. Shan and G. Doolen, "Multicomponent lattice Boltzmann model with interparticle interaction," J. Stat. Phys. **81**, 379 (1995).

[37] M. Sbragaglia, R. Benzi, L. Biferale, S. Succi, K. Sugiyama, and F. Toschi, "Generalized lattice Boltzmann method with multirange pseudopotential," Phys. Rev. E **75**, 026702 (2007).

[38] P. Yuan and L. Schaefer, "Equations of state in a lattice Boltzmann model," Phys. Fluids **18**, 042101 (2006).

[39] Z. Guo, C. Zheng, and B. Shi, "Discrete lattice effects on the forcing term in the lattice Boltzmann method," Phys. Rev. E **65**, 046308 (2002).

[40] Q. Li, K. H. Luo, and X. J. Li, "Forcing scheme in pseudopotential lattice Boltzmann model for multiphase flows," Phys. Rev. E **86**, 016709 (2012).

[41] A. J. Wagner, "Thermodynamic consistency of liquid-gas lattice Boltzmann simulations," Phys. Rev. E **74**, 056703 (2006).

[42] K. N. Premnath and S. Banerjee, "Incorporating forcing terms in cascaded lattice Boltzmann approach by method of central moments," Phys. Rev. E **80**, 036702 (2009).

[43] A. Gopinath and D. L. Koch, "Collision and rebound of small droplets in an incompressible continuum gas," J. Fluid Mech. **454**, 145 (2002).

[44] P. Zhang and C. K. Law, "An analysis of head-on droplet collision with large deformation in gaseous medium," Phys. Fluids **23**, 042102 (2011).